3D NUMERICAL MODELS FOR ALONG-AXIS VARIATIONS IN DIKING AT MID-OCEAN RIDGES

by

田小川

(Tian, Xiaochuan)

A Thesis

Submitted in Partial Fulfillment of the

Requirements for the Degree of

Master of Science

Major: Geophysics

The University of Memphis

May, 2015

Copyright © 2015 Xiaochuan Tian

All rights reserved

Dedication

I would like to dedicate this thesis to my mother, 田霞 (Tian, Xia). I wouldn't have a chance to experience this wonderful world without her giving birth to me. She rears me up by herself with her great love, optimism and peseverence. Without her guidance and support, I would not become who I am.

I also want to dedicate this thesis toward my major thesis advisor: Professor Eunseo Choi. His mentorship defines what a great advisor is like. Without his guidance, neither this thesis nor my fast personal development during these two years is possible. He has kindled a flame that illuminates the way for my future career as a geodynamic modeler.

Acknowledgements

There is no proper words for me to express my deep gratitude toward my thesis advisor, Professor Eunseo Choi. He has changed my life in a very positive way. From him, I have learned what a great researcher and educator should be like. It is because of his unfailing care and understanding that have given me the courage to persevere, and to carry on during the darkest days as an international student far away from home. It is his vivid and interesting lessons that have inspired me so much that I want to devote my career into geodynamic modeling. It is his numerous inspiration and encouragement that has motivated me to work super hard (enjoy at the same time) on the fascinating research questions. It is his altruistic share that has provided me with great chances to learn from great researchers, references, and to attend meetings. It is his patience to guide me through my endless silly questions that has nurished and cultivated my capabilities of being an independent researcher. Blessings from Eunseo, my role model, are countless. I will keep them in mind and try my best to relay the torch.

I would also like to thank members of my thesis committee, Professor Christine Powell and Professor Jer-Ming Chiu, for their guidance and support. Especially I want to thank Dr. Chiu for his sharing and advice on my course term projects and for his patience to answer all my silly questions. In addition, I want to thank Dr. Powell for your warm-hearted encouragement and benevolence during my studies at the Center for Earthquake Research and Information (CERI).

My sincere thanks must also go to the CERI and the University of Memphis (UM). Thanks a lot for providing me this great chance to study here with full tuition and graduate research assistanship. It is this kind support that has made my two-year studies at this great institution possible.

I am also grateful to the courses instructors for many vivid and interesting courses that have stimulated my interests in Geophysics, helped me build up my foundation and expanded my horizon in the field. They are Professor Robert Smalley for "Data Analysis in Geophysics”, Professor Charles Langston for “Global Seismology” and “Inverse Methods in Geophysics”, Professor Mitch Withers for “Signal Processing in Earth Science”, Professor Eunseo Choi for “Global Geophysics” and “Geodynamics”, Professor Christine Powell for “Evironmental Geophysics”, Professor Randy Cox for “Art of Earth Science”, Professor Jer-Ming Chiu for “Exploration Seismology”. Thank you so much. Especially, I want to thank Professor Withers for you encouragement and your time and efforts for answering all my questions. I would also like to thank Professor Eric Daub for your delicious homemade cakes provdided to our graduate students every Wednesday during the “CERI Discussion”. I am probably the person who ate most of them and enjoyed the most.

Many thanks must also go to my dear classmates and research colleagues, with whom, I have lived, studied and worked during the two years. Especially, I want to thank Yang Yang for your supportive help and share on several of my term projects. Thank you for being a wonderful roommate. I would also like to thank my best “cubic office mate”, Naeem Khoshnevis, for his best company. We’ve been studied together as the most diligent (long staying) people in CERI (12/7). Thank you for those benevolent and uncountable “how are you”, “good morning”, “good night” as well as many good chats. My sincere thank must also goes to Sabber Ahamed, who have been encouraging me during my darkest days when I lost direction. It is his enthusiastic share and encouragement that have helped me went through the bad days.

Special thanks must also go to CERI staffs. Thank you Chris McGoldrick for many of your kindly help and all the nice chats, from which I have learned many new English words and phrases. Thank you Tanya Broadbent and Kathleen Tucker for sending me birthday gifts which makes me feel so warm as being a member of CERI families. Thank you Christy Chiu and Jer-Ming Chiu for inviting me to your house for Chineses Spring Festival lunch which helped a lot in soothing my nostalgia for hometown. Thank you Gary Patterson for your share and benevolence. Thank you Deshone Marshall for constantly helping me out in using CERI's lab computers.

I also want to sincerely thank Center for Writing and Communication of the UM. Especially, I want to thank Bill Schraufnagel for your very supportive helps on revising this thesis and enhancing the presentation.

I also want to thank Professor 刘洁 (Liu, Jie) and Professor 张珂 (Zhang, Ke) from Sun Yat-sen University, for kindly sharing your computing resourses on Tianhe2 to me. Many thanks must also go to the staffs of Penguin, Stampede and Tianhe2 supercomputer centers, thank you so much for all the technical supports. Especially, I would like to thank National Supercomputer Center in Guangzhou, China, for providing me surpports with more than 200k of core-hours.

Sincere thanks must also go to the lifeguards and staffs of the swimming pool of the UM Recreation Center. Thank you for your work in providing me such a safe and enjoyable workout environments. Thank you for accompanying me almost everyday and making sure my safty during I am swimming. I could not endure all the stresses from the high pressure school works if without being able to enjoy swimming everyday.

In addition, I also want to express my sincere thank to Professor 成谷 (Cheng, Gu), my undergraduate thesis advisor. Thank you for providing me a chance to start my career as a geophysicist. Thank you for all you guidance and share.

I should never forget my deep gratitude to my middle school Math teacher 冯艳 (Feng, Yan) and high school Math teacher 陈胜方 (Chen, Shengfang) and Physics teacher 吕黎洁 (Lyu, Lijie). It is your great education, inspiration, love and care that have cultivated me into a person, who begins able to appreciate the fascinating science world. Your great efforts and patience in teaching me and answering my silly questions have helped me build up a good foundation for my future studies as a science major student.

Special thanks also go to a special person, 张思婉 (Zhang, Siwan). Thank you for planted a seed of love and beauty deeply in my heart that have been encouraging and inspiring me through time.

Finally, I want to thank my families. There simply is no proper word for expressing my gratitude. Thank you so much my dear grandfather 田升恒 (Tian, Shengheng), and grandmother 王德芬 (Wang, Defen), who have reared me up with great love and care. Thank you so much my grandgrandfather 田光宗 (Tian, Guangzong). I will never forget your last words for encouraging me to be a good person and a diligent student.

Thank you my dear mother, 田霞 (Tian, Xia). You are always a great mother to me. Thank you so much for rearing me up by yourself with your great courage, optimism, love and care. Without you, there is no me.

"In the midst of winter, I found there was, within me, an invincible summer."

—Albert Camus

"People have no higher calling than to strive for the greater good of humankind and society and that the future of humanity can be assured only when there is a balance between scientific development and the enrichment of the human spirit."

—Kazuo Inamori

"不失其所者久，死而不亡者寿。"

—《道德经》

Abstract

Tian, Xiaochuan. M.S. The University of Memphis. May 2015 Master of Science. 3D Numerical Models for Along-axis Variations in Diking at Mid-Ocean Ridges. Major Professor: Dr. Eunseo Choi.

Bathymetry reveals diverse morphologies at Mid-ocean Ridges (MORs). Previous studies show that the morphologies at slow spreading MORs are mainly controlled by the ratio (M) between rates of magma supply and plate extension. 2D models successfully explain many cross-sectional observations across the ridge axis. However, magma supply varies along the ridge and the interaction processes between the tectonics and magmatism at MORs are inevitably three dimensional. We investigate the consequences of this along-axis variation in diking in terms of faulting pattern and the associated structures with a 3D parallel geodynamic modeling code, SNAC. Many structural features observed are produced. We also proposed asynchronous faulting induced tensile failure as a new possibility for explaining corrugations. $\bar{M}$ =0.6425 is suggested as a boundary value for separating abyssal hills and oceanic core complexes (OCCs) formation. Previous inconsistency for OCCs formation between 2D model results (M = 0.3$\sim$0.5) and field observation that M can extends beyond the range is reconciled by our 3D along ridge coupling argument.

Table of Contents

List of Tables

List of Figures

1 Introduction

1.1 Review of Literature

Geodynamic modeling as well as a variety of geological, geophysical observations and lab experiments have provided insight into the processes occurring at the mid-ocean ridges (MORs) [e.g., Tucholke and Lin, 1994, Blackman et al., 2002, Behn et al., 2006, Behn and Ito, 2008, Ito and Behn, 2008, Baines et al., 2008, Escartín et al., 2008, Canales et al., 2008, Dick et al., 2008, Dannowski et al., 2010, Olive et al., 2010, Reston and Ranero, 2011, Reston and McDermott, 2011]. In particular, the advent of high-resolution multi-beam bathymetric data has made it possible to discover differences in axial topography between slow and fast spreading ridges and morphological transition from the center of a ridge segment to the tip of the ridge segment.

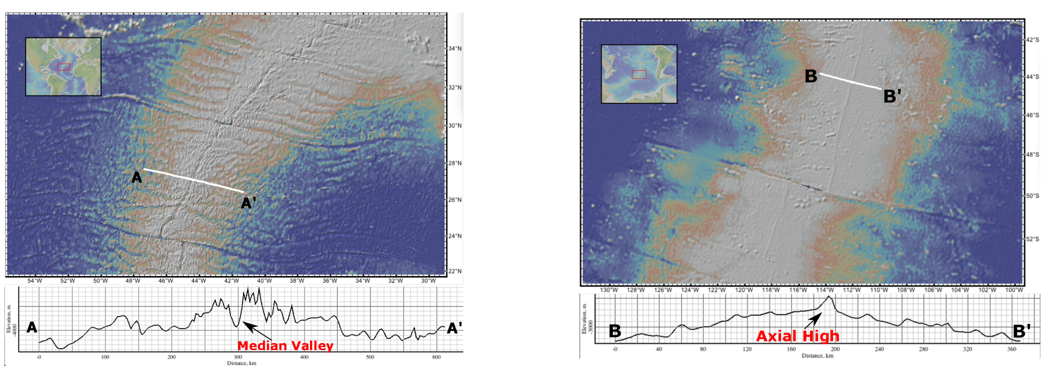

(a) Slow spreading Mid-Atlantic Ridge

(b) Fast spreading East Pacific Rise

Figure 1: Profiles of bathymetry across MORs.

Variations in morphologies among different MORs are mainly controlled by four factors: magma supply, tectonic strain, hydrothermal circulation and spreading rate [Fowler, 2004]. Among them, the spreading rate shows the strongest correlation with the ridge morphology. Slow-to-intermediate spreading ridges (half spreading rate less than 4 cm/yr) produce median valleys that are typically 10∼20 km wide and 1∼2 km deep (e.g., Mid-

Atlantic Ridges, Figure 1a). Fast-spreading ridges (half spreading rate greater than 5 cm/yr) like the East Pacific Rise have axial highs that are 10∼20 km wide, 0.3∼0.5 km high (Figure 1b).

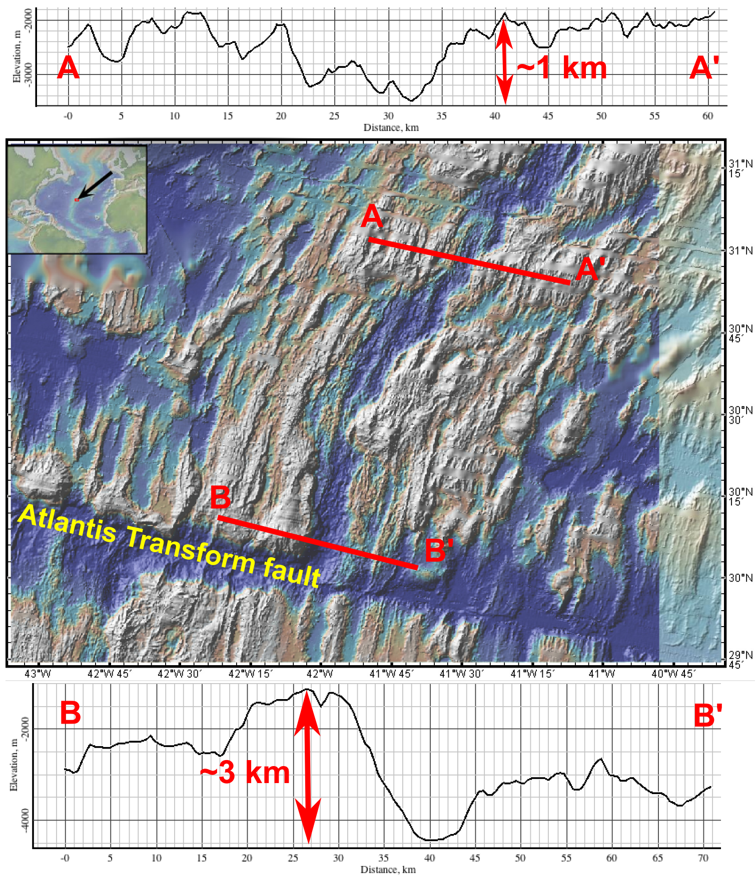

Figure 2: Two bathymetric profiles across the Mid-Atlantic Ridge around 30°N with vertical exaggeration of 10. A-A′ is closer to the segment center while B-B′ is at the tip of the segment.

Slow spreading ridges exhibit along-axis variations in off-axis morphology, the width and depth of median valleys and crustal thickness. Figure 2 shows that the topographic profile near to the center of the ridge segment (A-A′) is rather symmetrical and has a higher frequency with a median valley ∼12 km wide and ∼1 km deep. In constrast, the near-tip profile (B-B′) is asymmetrical and has a much lower frequency with a median valley wider than 30 km and shows a greater relief (∼3 km). The maximum along-axis

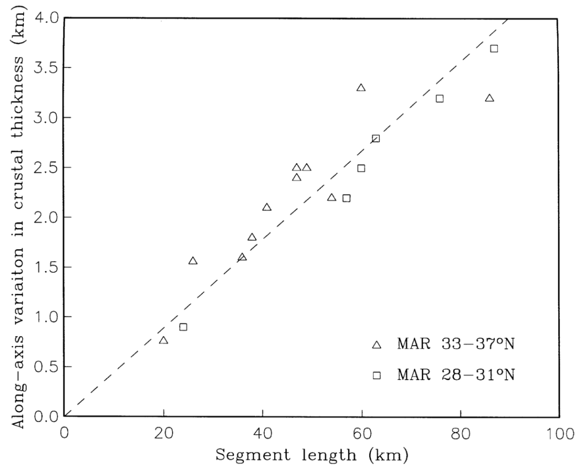

Figure 3: Relationship between the maximum crustal thickness variations (ΔH_c) along a ridge segment and the segment length (L). The dashed line is the best-fit linear regression of the combined data [Chen and Lin, 1999].

variation in crustal thickness ΔH_c is linearly increasing with segment length L [Chen and Lin, 1999] and the relationship is ΔH_c(L) = 0.0206L (Figure 3).

Magma supply at the MORs is mostly a passive process when no hot plume is present [Fowler, 2004]. Driven by both vertical pressure difference and buoyancy due to horizontal density difference, hot mantle rises up to fill the vacated room produced by the plate separation. Decompression of the upwelling hot mantle results in partial melting. The generated magma upwells to the upper crust and feeds the dikes at the ridge center.

The passive nature of the melting process at the MORs leads to the major difference between fast and slow spreading ridges. At fast spreading ridges, magma is generated at a higher rate than at slow spreading ridges. Thus, fast spreading ridges can sustain more frequent diking, which efficiently release stresses generated by far-field forces driving the plate motion. In contrast, diking is less frequent at slow spreading ridges and can only partially releases the stresses associated with plate motion. The plates associated with slow-spreading ridges experiences internal deformations (e.g. tectonics process like normal faulting) when the accummulated extensional stress exceeds the strength of the crust.

Buck et al. [2005] defined the ratio between the rate of plate separation by diking and spreading rate as M = $V_{dx}/2V_x$, where V_{dx} is the rate of opening by diking at the ridge center and V_x is the half spreading rate of the MOR. According to this definition, M = 1 represents the case where dike injection is so frequent that magma supply is sufficient to release all the tensional stresses from plate separation. M = 0 corresponds to the case of no magma supply, in which diking does not account for any of the plate motion and therefore plates kinematics requires plates to go through internal deformations. As shown in Figure 4, an axial high forms at a fast spreading ridge (M = 1) due to buoyancy from lateral density difference across ridge axis but a median valley forms at a slow-spreading ridge (M = 0.5) due to near-axis normal faulting, which is in turn caused by the stretching of oceanic lithosphere.

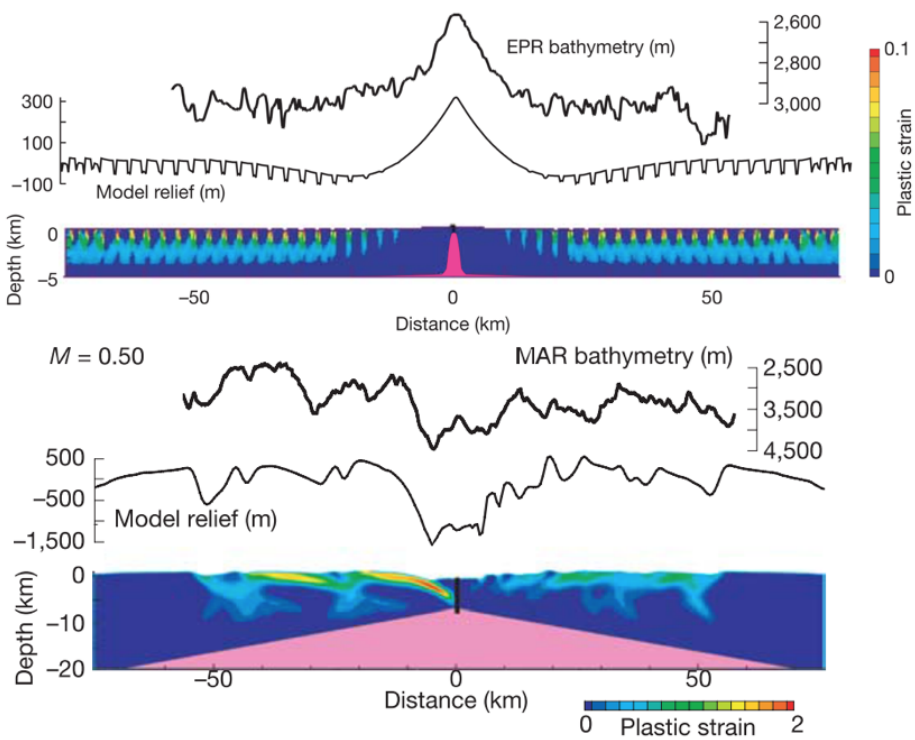

Figure 4: Upper one: modeling result for fast spreading agrees well with the observation of East Pacific Rise. Lower one: modeling result for slow spreading ridges agrees well with the bathymetry of Mid Atlantic Ridge. Adapted from [Buck et al., 2005].

Tucholke et al. [2008] expand the investigation on the role of M in the mid-ocean

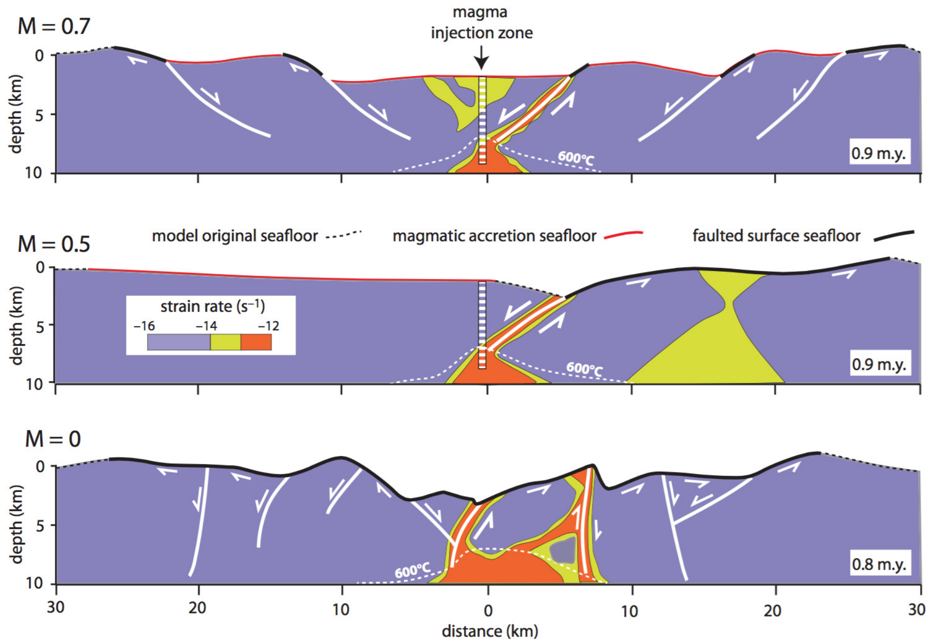

Figure 5: Snapshots of modeled fault behavior and seafloor morphology for values M = 0, 0.5, and 0.7; model allows thermal evolution. Structural interpretation is superimposed on modeled distribution of strain rate; model time is indicated in panels at lower right; dashed white line at bottom is 600 °C isotherm and approximates the brittle-ductile transition; dashed seafloor is original model seafloor, red seafloor is that formed dominantly by magmatic accretion, and solid bold seafloor is fault surface.[Tucholke et al., 2008, Whitney et al., 2012]

ridge mechanics. They focus on the faulting behaviors of slow spreading ridges and find that the OCCs are most likely to form when M varies from 0.3 to 0.5. When M = 0.7 (Fig. 5), repeated diking pushes faults that have formed at the spreading center away from the ridge axis. Since the thickness of the brittle layer increases away from the ridge axis due to cooling effects, frictional and bending energy for maintaining the fault also increases. When the energy needed for maintaining an existing fault exceeds the energy for breaking a new near-axis fault, the old fault is replaced by the new one and most of the extension is accommodated by the new fault. When M = 0.3∼0.5, the normal fault remains active for a long time and rotates to a low angle normal fault (detachment fault), exhuming the lower crust and mantle materials to the seafloor. When M $<$ 0.3, most of the tension is accommodated by intra-plate deformations rather than by diking and as a result, faulting pattern is more complicated and unsteady.

1.2 Statement of Research Purpose

The M-factor formulation used in the previous 2D models [e.g., Tucholke et al., 2008, Buck et al., 2005] successfully explained major features found in across-ridge profiles of seafloor bathymetry. However, 2D models have limitations in studying the along-ridge variations in morphology and faulting patterns. Magma supply at fast spreading ridges seems always sufficient for accommodating plate motions with little variation along the ridge axis. The relatively uniform topography along fast spreading ridges is considered to be consistent with the uniform abundance of the magma supply. However, along the slow spreading ridges, bathymetry, gravity anomaly and results from reflection and refraction seismology show strong correlation with variation in crustal thickness [e.g., Ryan et al., 2009, Chen and Lin, 1999, Lin et al., 1990, Tolstoy et al., 1993]. Because oceanic crust is mainly formed by upwelled magma at the ridge, variation in the thickness of the crust implies variation in magma supply. At slow spreading ridges, the degree of cooling by hydrothermal circulation, thermal structures and even local spreading rate [Baines et al., 2008] also varies both along and across the ridge axis and they appear interrelated. Thus, for slow-to-intermediate spreading ridges, the interactions between tectonics and magmatism at MORs are inevitably 3D processes and 3D numerical models are desirable for better understanding factors controlling both across- and along-ridge morphology variations.

The purpose of this thesis is to extend the M-factor formulation originally developed for 2D models to three dimensions (3D) by implementing it into a 3D numerical modeling code SNAC (**S**tGermai**N** **A**nalysis of **C**ontinua) [Choi et al., 2008]. By systematically exploring the behaviors of the 3D models and comparing them with observations, we aim to better understand how the mid-ocean ridge magmatism and tectonic deformations interact.

2 Methods

2.1 Method of approach

The numerical modeling code, SNAC (**S**tGermai**N** **A**nalysis of **C**ontinua), is an explicit Lagrangian finite element code that solves the force and energy balance equations for elasto-visco-plastic materials. Figure 6 shows major components of SNAC.

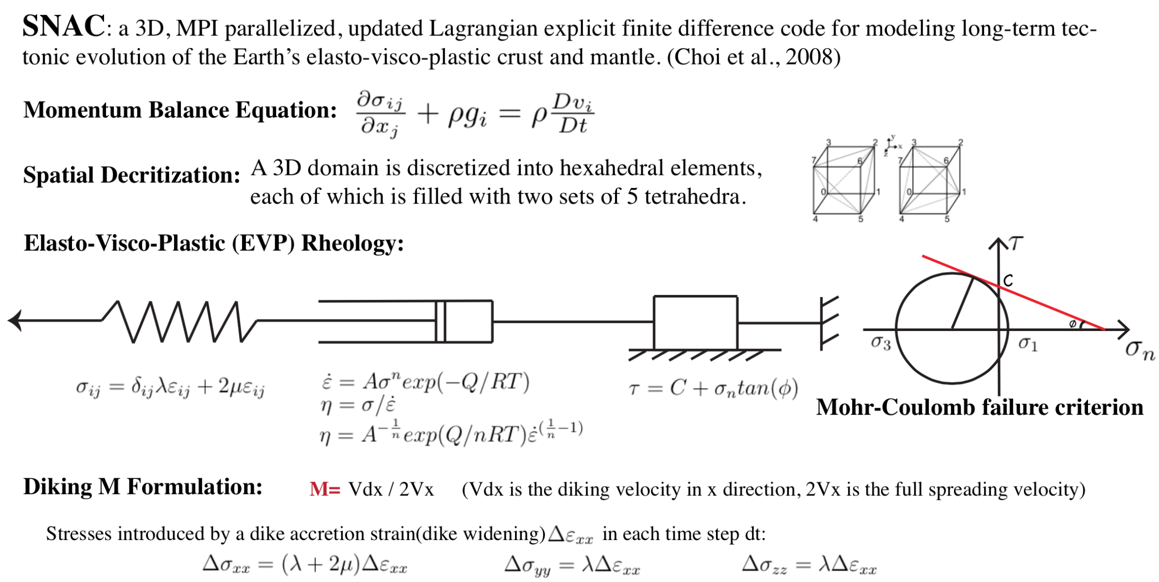

Figure 6: Essential components of the numerical method.

For each time step, strain and strain rates are updated based on the initial or previous velocity fields under the constraints from boundary conditions. A constitutive model returns updated stresses corresponding to these deformation measures. Internal forces are then calculated from the updated stresses, which is plugged into the momentum balance equation together with the body force term. Then, the damped net force divided by inertial mass yields acceleration at a node point, which is time-integrated to velocity and displacement.

A 3D domain is discretized into hexahedral elements, each of which is in turn divided into two sets of tetrahedra. This symmetric discretization prevents faulting from favoring a specific direction or “mesh grains”.

Rheology for the oceanic lithosphere is assumed to be elasto-visco-plastic (EVP). When viscosity is high at low temperature, the EVP rheology implemented in SNAC essentially becomes the Mohr-Coulomb plasticity with strain softening that can create shear bands that behave like faults. Strain softening is realized by cohesion decreasing with increasing amount of permanent (i.e., plastic) strain. I assume this relationship is linear for simplicity. It is sufficient for a full description of such a linear strain weakening to define initial and final values of cohesion and a critical plastic strain at which cohesion becomes the final value. I define the rate of strain weakening as the cohesion difference divided by the critical plastic strain and use it as one of the model parameters. When temperature is high and viscosity is low, the rheology becomes the Maxwell viscoelasticity and can model creeping flow. This property of the EVP model makes it possible to set up a structure with a brittle lithosphere and a ductile asthenosphere through a proper temperature distribution. Rheological parameters are taken from previous studies that use a similar rheology [e.g., Buck et al., 2005; Tucholke et al., 2008] or from lab experiments [e.g., Kirby and Kronenberg, 1987].

For 3D diking processs, the strain $\Delta\varepsilon_{xx}$ associated with diking leads to stresses changes, $\Delta\sigma_{xx}$, $\Delta\sigma_{yy}$ and $\Delta\sigma_{zz}$. These stress changes due to diking are computed according to the linear elastic constitutive equations $\sigma_{ij} = \lambda\varepsilon_{kk}\delta_{ij} + 2\mu\varepsilon_{ij}$.

2.2 Model Setup

The 3D models have a common geometry of 60 km $\times$ 20 km $\times$ 20 km in x, y and z axes respectively with a resolution (Δx) of 1 km (i.e., Δx is the size of each hexahedron element)(Fig. 7). The initial temperature field linearly increases from 0 °C at the top surface to 240 °C at the depth of 6 km, reflecting enhanced cooling due to hydrothermal circulation. Below 6 km, the temperature profile follows the semi-infinite half-space cooling model of moving plates [e.g., Turcotte and Schubert, 2002]. Two sides perpendicular

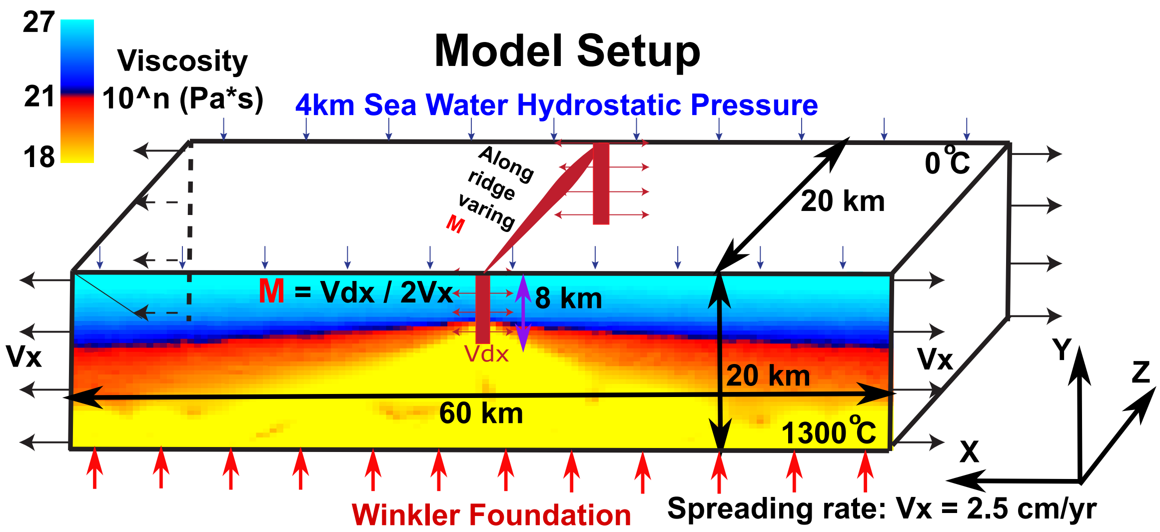

Figure 7: Model setup.

to the z coordinate axis are free-slip. The top surface has vertical tractions from water columns, of which heights are locally determined as (4000 - $h(x, z)$) m, where $h(x, z)$ is the topography at a location, (x, z). The bottom surface is supported by the Winkler foundation. Temperature is fixed at 0 °C on the top surface and at 1300 °C on the bottom surface.

Diking, represented by the factor M as described above, is assumed to occur in the middle of the doamin (Fig. 7), where the lithosphere is the thinnest.

We adopt the linear isotropic elasticity, power-law viscosity of dry diabase [e.g., Kirby and Kronenberg, 1987, Buck et al., 2005] and the Mohr-Coulomb plastic model. The complete list of model parameters are given in Table 2.

Before running 3D models, I have run hundreds of pseudo-2D models for initial setup and benchmarking with previous studies [e.g., Buck et al., 2005, Tucholke et al., 2008]. Preliminary pseudo-2D results show that the model behavior in faulting pattern is sensitive to the rate of strain weakening. Two cases of strain weakening are tested in the 3D models. In one case (denoted as Type 1 weakening), cohesion linearly decreases from 44 MPa (denoted as C_i) to 4 MPa (C_e) for plastic strain accumulating from 0 ($\varepsilon^1_{p_i}$) to 0.1 ($\varepsilon^1_{p_e}$). It has a characteristic fault slip of 150 m for pseudo-2D models and 300 m for 3D models. The other case (Type 2 weakening) assumes cohesion linearly decreasing from 44 MPa (C_i) to 4 MPa (C_e) for plastic strain accumulating from 0 ($\varepsilon^2_{p_i}$) to 0.33 ($\varepsilon^2_{p_e}$). In this case, the characteristic fault slip for pseudo-2D models is 500 m and for 3D models is 1 km. The characteristic fault slip is defined as ΔX_c=3$\Delta x \varepsilon_{p_e}$ where 3 Δx represents the thickness of the shear bands which is usually 2 to 4 times Δx (size of a hexahedron element) [Lavier et al., 2000]. When ΔX_c amount of slip takes place at the fault interface, the cohesion of the material at the faulting interface decreases to C_e. In this way, under the same amount of ΔX_c, models with different resolution should produce the same faulting patterns.

Although how to estimate the M values from observations is a subject of on-going research, constraints are available from a large dataset of bathymetry, gravity and seismic surveys as well as geological drilling. Generally, at slow spreading ridges, magma supplies mostly at the center of the ridge segment and decreases towards the tip of the segment [e.g., Tolstoy et al., 1993, Chen and Lin, 1999, Carbotte et al., 2015]. There is also evidence for shorter wavelength of 10 to 20 km discrete focus of magma accretion along the ridge axis [Lin et al., 1990].

The numerical cost of a 3D model is non-trivial. For 2 Myr of model time, each model usually runs on 192 cores for about 48 hours (i.e., around 10^4 core-hours).

Based on these observational constraints and computational cost, I start considering a few scenarios of variations in M along the ridge axis. They are 1) three types of functional forms, linear, sinusoidal and square root; 2) three ranges of M variation along the ridge axis, 0.5 to 0.7, 0.5 to 0.8 and 0.2 to 0.8; and 3) two types of weakening rate, type 1 and type 2.

While 18 models are possible, I could run 15 models with the available computational resources. The complete list of the models is given in Table 1.

Table 1: List of 3D numerical experiments.

Model	M range	Functional Form	Type of weakening	For short
1	0.2-0.8	Linear	Type 1	M28LinT1
2	0.2-0.8	Sinusoidal	Type 1	M28SinT1
3	0.2-0.8	Square Root	Type 1	M28SqrtT1
4	0.5-0.7	Linear	Type 1	M57LinT1
5	0.5-0.7	Sinusoidal	Type 1	M57SinT1
6	0.5-0.7	Square Root	Type 1	M57SqrtT1
7	0.5-0.7	Linear	Type 2	M57LinT2
8	0.5-0.7	Sinusoidal	Type 2	M57SinT2
9	0.5-0.7	Square Root	Type 2	M57SqrtT2
10	0.5-0.8	Sinusoidal	Type 1	M58SinT1
11	0.5-0.8	Square Root	Type 1	M58SqrtT1
12	0.5-0.8	Linear	Type 2	M58LinT2
13	0.5-0.8	Sinusoidal	Type 2	M58SinT2
14	0.5-0.8	Square Root	Type 2	M58SqrtT2
15	0.8-0.8	Constant	Type 2	M88ConT2

Table 2: Summary of 3D Model Parameters

Number	Variable	Description	Value	Units
1	W_{dike}	Dike width	2	km
2	D_{dike}	Dike depth	8	km
3	H	Crustal thickness at dike	6	km
4	dT/dy	Crustal thermal gradient	40	K/km
5	T_1	Temperature at lower boundary of crust	240	$°C$
6	g	Gravity acceleration	10	m/s^2
7	$demf$	Dimensionless force damping factor	0.8	N/A
8	dt	Time step	1.5768e+07	$second$
9	$topo_kappa$	Parameter for topography smoothing	0	N/A
10	$shadowDepth$	Ghost elements for parallel computing	2	N/A
11	$meshI$	Mesh number in X direction	60	N/A
12	$meshJ$	Mesh number in Y direction	20	N/A
13	$meshK$	Mesh number in Z direction	20	N/A
14	L_I	Length in X direction	20	km
15	L_J	Length in Y direction	20	km
16	L_K	Length in Z direction	20	km
17	ρ	Density	3000	kg/m^3
18	λ	Lam$\acute{e}$'s constant	30	Gpa
19	μ	Shear modulus	30	Gpa
20	$refvisc$	Reference viscosity	0.125e-17	Pa^{-n}/s
21	$activationE$	Activation Energy	276.0e+3	kJ/mol
22	vis_{min}	viscosity minimum cutoff	1.0e+18	$Pa * s$
23	vis_{max}	viscosity maximum cutoff	1.0e+27	$Pa * s$
24	$srexponent$	Power of power law in viscosity	3.05	N/A
25	$\varepsilon^1_{p_i}$	initial plastic strain for piecewise Type 1 weakening	0	N/A
26	$\varepsilon^2_{p_i}$	initial plastic strain for piecewise Type 2 weakening	0	N/A
27	$\varepsilon^1_{p_e}$	end plastic strain for piecewise Type 1 weakening	0.1	N/A
28	$\varepsilon^2_{p_e}$	end plastic strain for piecewise Type 2 weakening	0.33	N/A
29	C_i	initial Cohesion for piecewise weakening	44	Mpa
30	C_e	end Cohesion for piecewise weakening	4	Mpa
31	ϕ	Friction angle	30	$°$
32	$remesh_{timestep}$	Remesh when timestep reach its value	400000	N/A
33	$remesh_{length}$	Remesh when the global minimum of the ratio of the volume of a tetrahedron to one of its surface area	0.6	N/A
34	top_{Temp}	Surface temperature	0	$°C$
35	$bottom_{Temp}$	Bottom temperature	1300	$°C$
36	V_x	Half spreading rate	7.9e-10	m/s

3 Results

3.1 Reference model

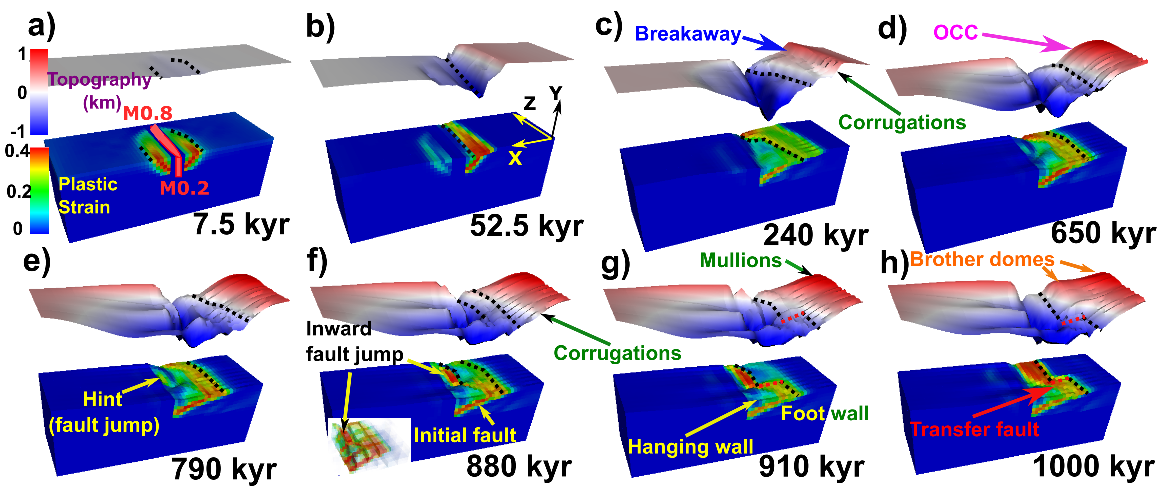

Figure 8: Evolution of plastic strain and surface topography of the reference model M28LinT1. Each snapshot shows plastic strain plotted on the model domain, the five times vertically exaggerated topography and the time at which it is taken. The initial seafloor is at 0 km of elevation. The black dashed lines are the terminations of faults. The red dashed lines in g) and h) are the transfer faults that connect the terminations. The inset in f) plots plastic strain with opacity linearly proportional to plastic strain value.

I consider the model with M varying linearly from 0.2 to 0.8 along the ridge axis with type 1 weakening rate as the reference model and denote it as M28LinT1 following the shorthand notations given in Table 1. I describe the general model behaviors in this section and then provide details and mechanisms of the major structural features of the model in the next section.

For the first 7.5 kyr (Figure 8.a), normal faults, represented by localized plastic strain, begin to form near the ridge axis. Because stresses due to plate extension accummulate faster at the lower M side than at the higher M side, faults first initiate at the lower M side and then propagate to the higher M side. Such an asynchronous initiation of faults along the ridge axis creates offset in breakaway at later stages, i.e., the breakaway at the lower

M side moves further away from the ridge axis than that of the higher M side (Figure 9).

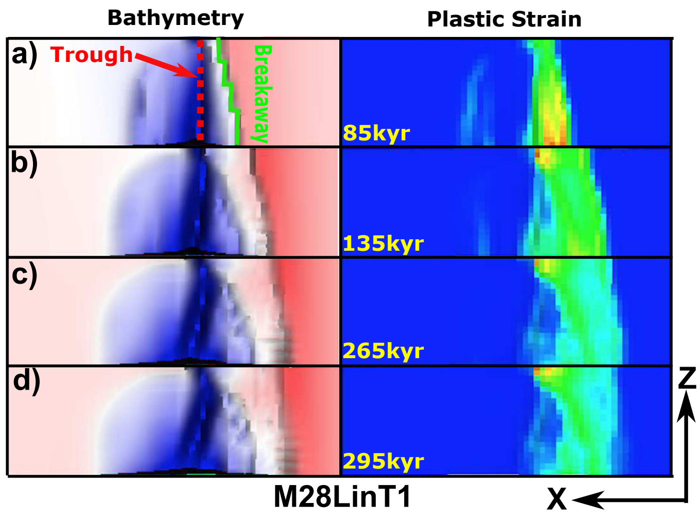

Figure 9: Bird's eye view of a breakaway in the reference model at a) 85 kyr, b) 135 kyr, c) 265 kyr and d) 295 kyr. The breakaway is marked by green solid line in a). A narrow zone of depressed topography ("trough") is marked by red dashed line inside the medain valley (blue area) in a). Color scales are the same with those in Figure 8.

Likewise, the model produces a median valley that widens and deepens with rates inversely proportional to the M value (i.e. rate of local magma supply) (Fig. 8a-c; Fig. 9a-d).

By 52.5 kyr (Figure 8.b), the normal fault on the right hand side of the ridge axis remains active while the one on the left becomes inactive. As the active fault slips, crust at the footwall bends in a clockwise rotation as is illustrated in Figure 10. The upper part of the active fault plane (shown as plastic strain in the model) is exposed to the seafloor.

The active normal fault on the right rotates to a lower dip of $\sim$30 $^\circ$ at the root of the fault and to $\sim$0 $^\circ$ at the exposed fault interface after about 240 kyrs (Fig. 8.c). However, the normal fault at the higher M side (especially for $M > 0.7$) experiences less fault rotation and the termination of the fault is closer to the ridge axis. The maximum relief between the breakaway and the trough inside the median valley becomes larger than 1 km. In addition, $\sim$2 km wavelength corrugations begin to form between the breakaway and

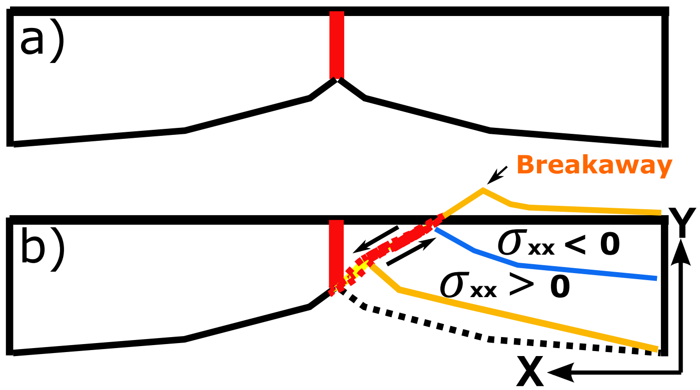

Figure 10: Illustration of the development of bending stress in lithosphere associated with faulting at the MOR. The blue line is the neutral plane where $\sigma_{xx} = 0$. Above the neutral plane is compression ($\sigma_{xx} < 0$) and beneath it is tension ($\sigma_{xx} > 0$).

termination at the lower M side (M < 0.35). I discuss the formation mechanism for the corrugations in Discussion.

By 650 kyr (Figure 8.d), the detachment fault reaches its lowest dip angle and its termination stops moving away from the ridge axis. The original breakaway of this detachment has already moved out of the model domain. The total fault offset at this point is greater than the thickness of the crust and thus would be sufficient for exhuming the upper mantle materials.

A new near-axis fault first appears at the center of the model domain with M $\in$ (0.5, 0.65) and then propagates in a positive z direction (Fig. 8.d,e). At this time, the initial detachment fault is still active and takes up most of the extension.

The new near-axis normal fault at the higher M side cuts through the hanging wall of the detachment fault at 880 kyr (Fig. 8.f). It coexists with the initial detachment fault and begins to accommodate most of the intra-plate extension. This event is called the "inward fault jump" [Tucholke et al., 1998; Dick et al., 2008].

By 910 kyr (Fig. 8.g), the inward fault jump completes in the M > 0.5 region: the new high-angle fault takes up all the extension and the initial detachment fault becomes completely inactive. The block that was previously a hanging wall to the detachment becomes a footwall of the new fault, passively moving with the plate to the negative x-axis direc-

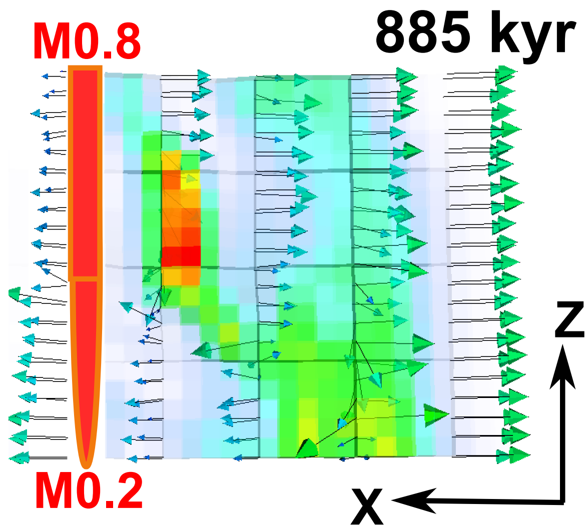

Figure 11: Bird's-eye view of velocity field with plastic strain ploted with opacity linearly proportional to its value. (color scale is the same as Figure 8.a))

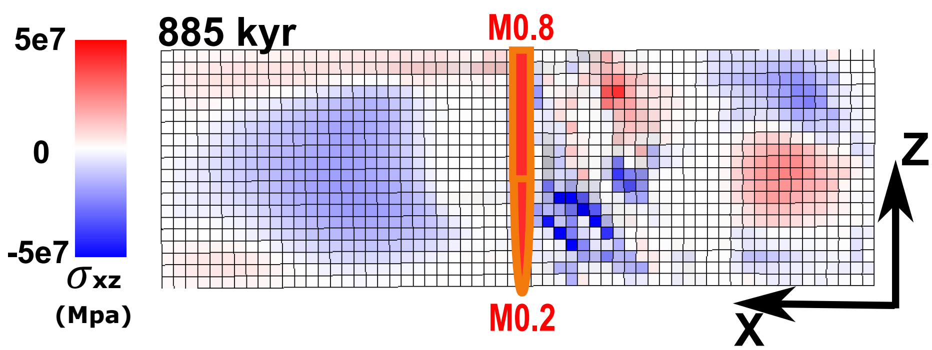

Figure 12: Bird's eye view of σ_{xz}.

tion. At the lower M side, the detachments is still active and the hanging wall continues to move toward the positive x-axis direction (Figure 11). This dextral sense of relative motions between the high and the low M side produces a region of sinistral shear stress σ_{xz} (Figure 12) and eventually creates a transfer fault (Fig. 8.h). As the inward jumped fault evolves, another dome ajacent to the initial OCC is produced at the higher M side by 1000 kyr.

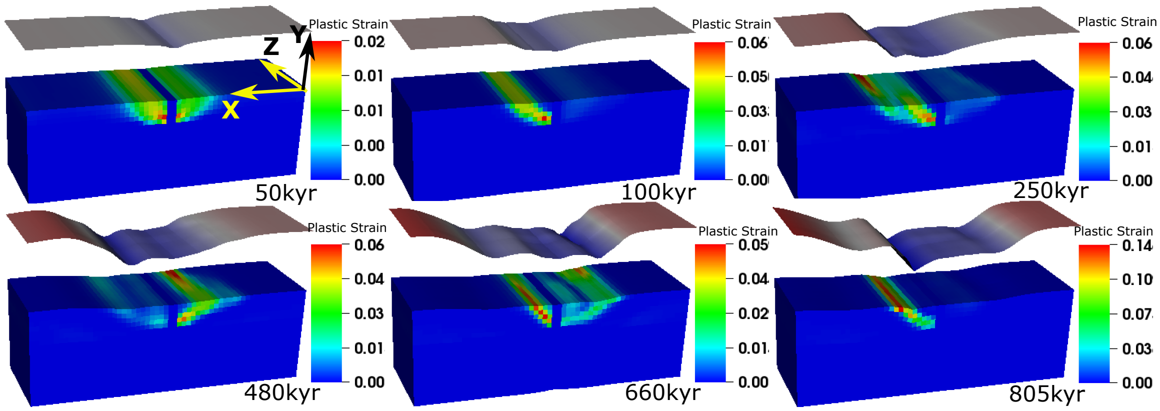

Figure 13: Evolution of plastic strain and surface topography of the model: M88ConT2 (Table 1). (color scale of topography is the same as Figure 8.a)

3.1.1 Constant M model M88ConT2

As a comparison to the varying M models, a constant M model is run. It shows similar behaviors with a corresponding 2D model from the previous studies and does not show along-ridge variations in terms of morphology and faulting.

As shown in Figure 13, model M88ConT2 pruduces a ∼20 km wide and 1∼2 km deep median valley, which is similar to the generally observation of the Mid-Atlantic Ridges. The width and depth of the median valley is almost constant along the ridge as contrast to the varying M models. The variation of the location of the breakaway and termination along the ridge that is mentioned in the reference model (M28LinT1) does not show up. Because the magma supply is constant along the ridge with M = 0.8, there is no stress perturbation along the ridge. Thus, the normal faults along the ridge initiate at the same time and the slipping rate of the fault is also constant along the ridge axis. The synchronized fault initiation results in no offset between breakaways and the constant sliping rate produces no along ridge axis variation in the position of the termination. In addition, neither corrugations nor mullion structures are generated. Normal faults alternate on each side of the ridge axis with a period of ∼10 km. This fault alternaltion produces symmetrical high frequncy abyssal hills.

3.2 Main structural characteristics

I describe seven structural characteristics of the reference model: Location of the termination, geometry of the trough, inward fault jump, fault alternation, mass wasting, hourglass-shaped median valley and corrugations and mullion structures. Since the details of these features differ among the models, they are useful for delineating and contrasting complicated model behaviors.

3.2.1 Location of termination

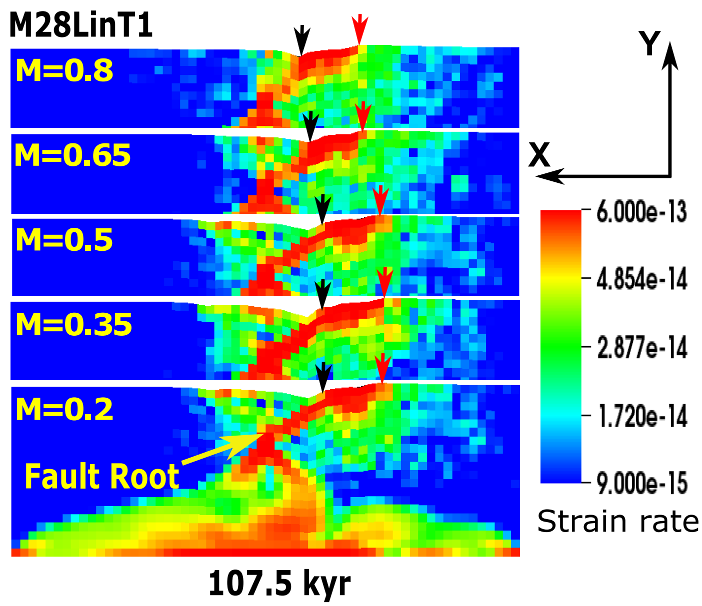

Figure 14: The second invariant of strain rates plotted on the reference model's vertical cross-sections along the ridge at 107.5 kyr. Terminations and breakaways are marked by black and red arrows.

Location of a fault termination varies along the ridge as indicated by black dashed lines in Figure 8 and black arrows in Figure 14. The highest strain rate regions (red) in Figure 14 can be interpreted as the active detachment fault interfaces. Compared to the two slices with M $>$ 0.5, the distances between terminations and the ridge axis at the lower M side (M $<=$ 0.5) is larger and the dip angles of the detachment faults are lower.

For ridge region with M $>$ 0.5, the fault root is pushed away from the ridge axis due to excessive diking while the termination is closer to the ridge axis due to lower slipping rate of the fault and the asynchronous initiation of faulting along the ridge. Thus the distance between the termination and the fault root is smaller at the higher M side and the dip angle of the fault is higher. However, among the three slices of M $<=$ 0.5, the distances and the dip angles are similar. Since the detachment faults for the ridge region with M $<$ 0.5 root at the same place at the intersection between the center dike and the brittle-ductile transition (BDT), although the rate of fault slip is higher for lower M, the rotation rate of the detachment fault interface is the same. Because it is only determined by how fast the termination moves away from the fault root. Since the moving rate of the termination has a maximum value that is restricted by the far field extension rate V_x, the bending rates of the detachment faults is similar among the three slices of M $<=$ 0.5.

One thing needs to be noted is that the trough at the higher M side correspond to the terminations but detached from the terminations at the low M side (M $<$ 0.5) as shown in Figure 14.

3.2.2 Geometry of trough

The depressed narrow region that developes in the median valley is termed as "trough". The reference model showed that its shape in the bird's eye view evolves from a straight line parallel to the ridge axis to a line oblique to the ridge axis (Figure 9.a-d). Initially, the trough along the ridge corresponds to the termination. However, at the lower M side (M $<$ 0.5), as the normal fault rotates to a lower dip at the lower M side, the trough is no longer coincident with the fault termination and is moving slowly to the left because the hanging wall is pulled by the conjugate plate. However, the trough on the higher M side (M $>$ 0.5) is pushed away from the ridge axis [Tucholke et al., 2008]. But since the trough cannot bypass the termination, the trough at M = 0.8 is restricted closer to the ridge axis. Together it generates the curved shape of the trough (Figure 9.d).

3.2.3 Inward fault jump

The inward fault jump (e.g., Fig. 8) occurs in most of the models when the energy for mainting an old fault becomes larger than breaking a new one near the ridge axis. As shown in Figure 14, at the region with M > 0.5, the existing normal fault is pushed away from the ridge-axis due to robust diking (M > 0.5). As it moves away from the ridge axis, the frictional energy for the fault, the bending energy for the footwall as well as the negative work done by gravity that resists the exhumation of the footwall increase [Lavier et al., 2000, Olive et al., 2014]. The initial detachment fault remains active until the negative works reach an upper limit that breaking a new fault near the ridge axis needs less work than to maintain the initial one, the initial detachment fault at the higher M side is then substituted by the inward jumping fault that cuts through the previous hanging wall. As the fault evolves, it connects to the initial detachment at the lower M side (M < 0.5) by a transfer fault and generates a curved termination along the ridge. Unlike fault alternation described below, the inward fault jump occurs on the same side of the ridge axis with its along-axis extent corresponds to the M > 0.5 region.

3.2.4 Fault alternation

Fault alternation is the behavior of normal faults alternatively show up on each side of the ridge axis when magma supply is robust enough. As shown in M88ConT2 (Figure 13). The normal fault first evolves on the left hand side of the ridge axis and produces an abyssal hill parallel to the ridge axis. By 480 kyr, another normal fault evolves on the other side of the ridge axis and takes the place of the first one. Note that among the 15 models (Table 1), only three produce fault alternation. They are M88ConT2, M58SinT2 and M58SqrtT2. Fault alternates only when weakening rate is low (type 2 weakening) and the average integration of M along the ridge is larger than 0.65. Analysis on when and why fault alternates is given in the Discussion section.

3.2.5 Mass wasting

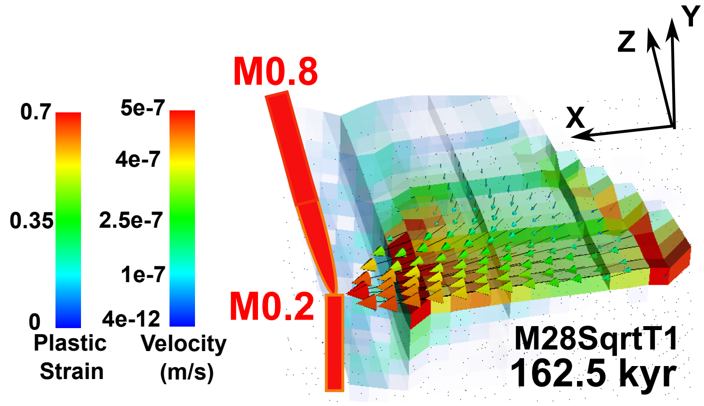

Figure 15: Velocity of the mass wasting hanging wall. Magnitudes of the velocity are shown by the colors of the arrow heads. Plastic strain is plotted with opacity linearly proportional to its value.

Mass wasting occurs on the exposed surface of a low-angle normal fault. When the weak fault zone becomes gravitationally unstable and is detached from the underlying material, the detached layer flows towards the lower elevated ridge axis and the lower M side driven by gravity with a velocity ∼10 times faster than the half spreading rate (Figure 15; Figure 17.b,e (first row))). As the top layer of the hanging wall flows down the topography slope, obvious topography drop is observed in 2.5 kyr (Figure 17.b) versus c); d) versus e) (topography)).

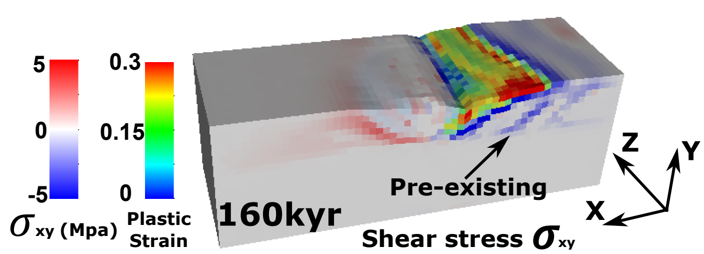

Figure 16: The weak detachment fault tip reaches the pre-existing shear stress. Plastic strain is plotted with opacity linearly proportional to its value.

Mass wasting is triggered by several factors. First, when the tip of the weak fault interface moves away from the ridge axis with the spreading plate and is intersected by a pre-exisitng shear stress σ_{xy} (Figure 16), the extra shear stress cuts the tip of the weak fault interface and leads to the decoupling between the breakaway and the upper layer of the hanging wall of the detachment fault. Second, during the roll over of the hanging wall at the breakaway, tensional stress ($\sigma_{xx} > 0$) promotes the deviatoric stress for generating small scale high angle normal faults cutting detachment fault surface [Tucholke et al., 1998] (Figure 31.c,d) and in this case the tip of the weak layer. In addition, along ridge coupling tends to resist the increase in along ridge offset of breakway which is generated by along ridge varying slip rates of the faults. As Figure 31 shows, the sinistral sense shear stresses (red σ_{xz}) beneath the top weak layer tends to rotate the upper layer and assists in triggering the decoupling process.

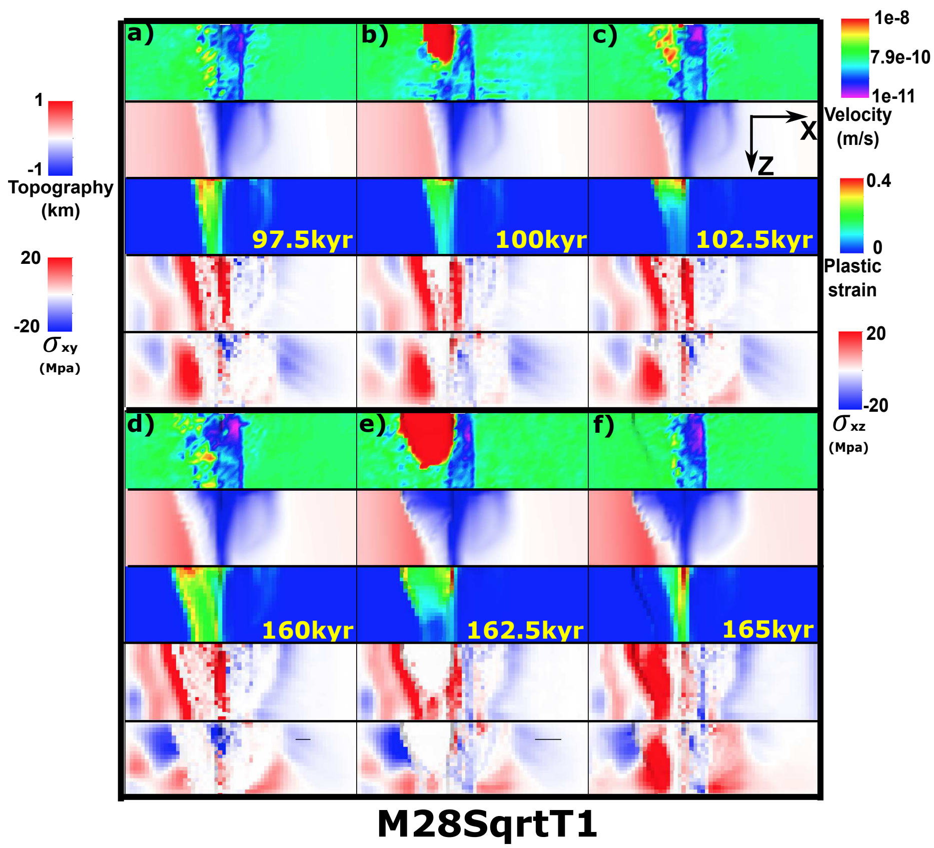

Figure 17: Plastic strain, topography and stresses evolution for M28SqrtT1.

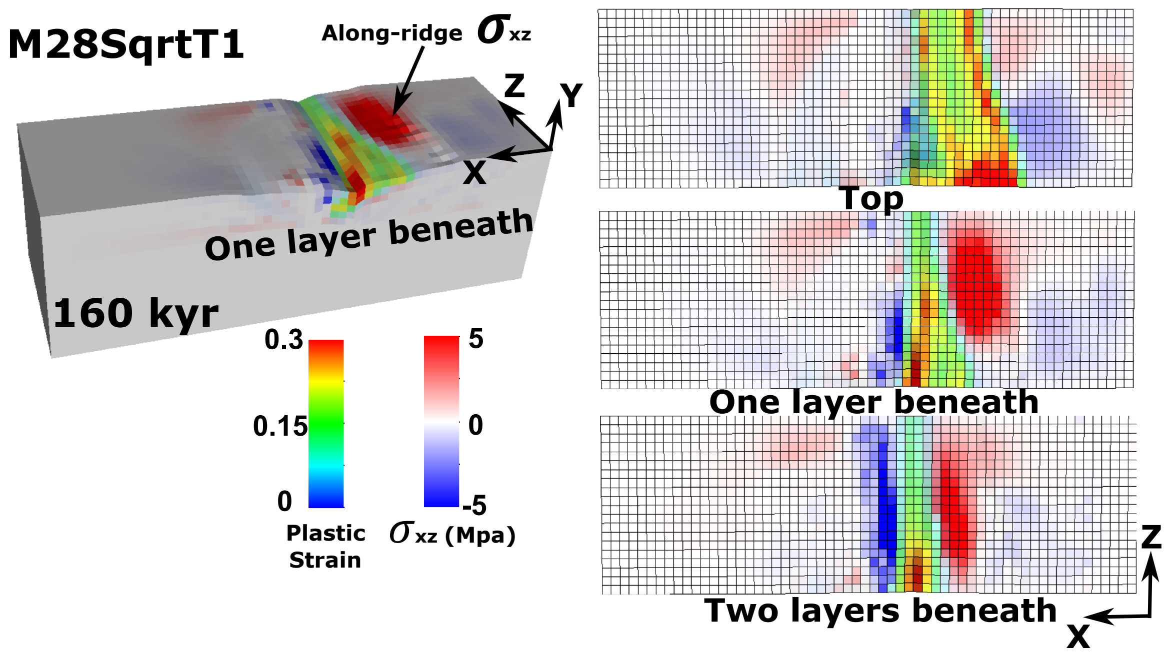

Figure 18: Along ridge axis σ_{xz} (bird's-eye view of three layers of model domain) (positive(red) means clockwise). Plastic strain is plotted with opacity linearly proportional to its value.

3.2.6 Hourglass-shaped median valley

All the models with M variation develop an hourgalss-shaped median valley although the geometry of the median valley changes with time and with the functional form of M variation. A median valley of the M28Sqrt model initially has a uniform width along the ridge but is deeper on the lower M side where normal faults first form (Figure 19.a). By $\sim$100 kyr, the fault on right hand side of the ridge axis does not propagate to the higher M side of the ridge and becomes inactive (Figure 19.b). It produces a depressed topography curve following the inactive fault trace, which is further away from the ridge axis at the lower M side but closer to ridge axis at the higher M side. On the other side of the ridge axis, as the active fault rotates to a lower dip angle, breakaways at the lower M side moves further away from the ridge axis than the breakaway at the higher M side. This along-ridge variation in the location of the breakaways act as another boundary of the hourglass on the

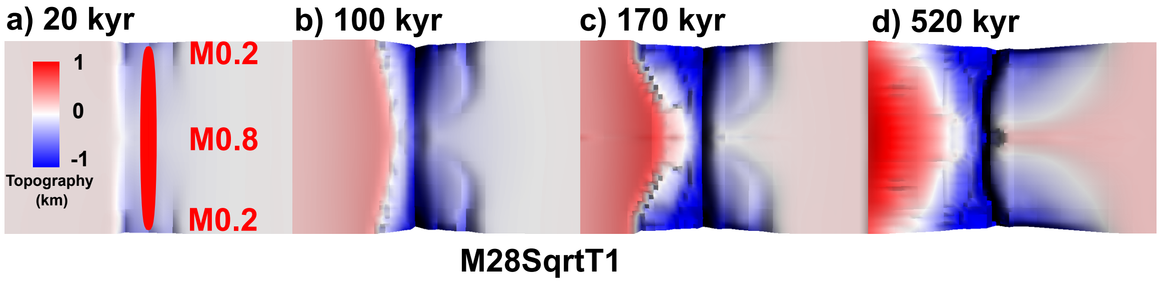

Figure 19: Bird's-eye view of the evolution of the hourglass shape median valley. It is generated by attaching the topography of the M28SqrtT1 model to its mirror reflection by assumming symmetrical M variation (0.2 to 0.8 to 0.2).

left. By ∼170 kyr (Figure 19.c), the hourglass-shaped median valley continues to widen and deepen. Since the area of the cross-section along the ridge inside the hourglass shape median valley is approximately inversely proportional to the local M values, the shape of the hourglass varies with different ranges and functional forms of M variations.

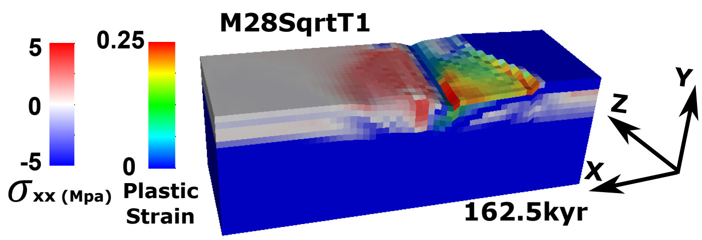

Figure 20: Higher σ_{xx} shows inside the median valley on the negative x-axis direction of the ridge axis.

In addition, the further depression inside the median valley is mostly due to the elastic deformation from crustal extension. As shown in Figure 20, the σ_{xx} in the median valley is higher because that the brittle crust is the thinnest at the median valley, when same amount of force propagates from far field extension to the median valley, the stress increases. This increased σ_{xx} is responsible for the further depression and extension of the median valley on the side of the ridge axis with no active faulting (Figure 19.d). For the median valley on the other side of the ridge axis, mass wasting between the breakaways and the ridge axis results in the further lowering in topography (Figure 17.d versus e (topography)).

3.2.7 Corrugations and mullion structures

Both corrugations and mullion structures are linear structures parallel to the spreading direction. As shown in Figure 8.f, at the M < 0.5 area on top of the OCC surface, corrugations show a uniform wavelength of ~2 km with hundreds of meters in amplitude. While at the higher M side of the ridge (Figure 8.g), a mullion structure of a wavelength of ~7 km shows up on the surface of the OCC. In spite of morphological similarity, corrugations and mullion structures have different formation mechanisms.

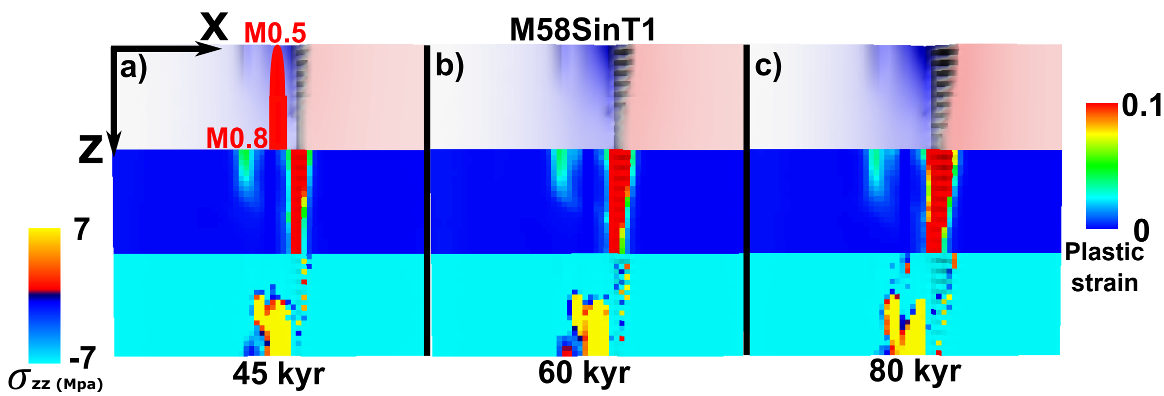

Figure 21: Bird's eye view of the evolution of the corrugations. Color scales for the topography is the same as Figure 8.

Corrugations

The corrugation starts at the breakaway as a response to tensile stress in the z-axis direction. As shown in Figure 21, when the plastic strain reaches or excedes 0.1 (red color), base on type 1 weakening, the cohesion decreases to 4 Mpa. With a 30 ° friction angle, tensile failure is declared when the σ_{zz} reaches ~7 Mpa (yellow color). The tensile stress is generated by the asynchronous faulting along the ridge. Faulting initiates earlier at the lower M side of the ridge. As the fault offsets more on the lower M side than on the higher M side, the footwall of the fault rotates and get uplifted more on the lower M side. This relative displacement between the footwalls along the ridge generates the isochron-parallel tesional stress σ_{zz}. Since σ_{zz} follows along the moving tip of the plastic strain, the plastic srain together with σ_{zz} generate tensile failure that extends away from the ridge axis and thus produces the linear corrugations that are parallel to the spreading velocity. Detail analysis along with simpler model experiments are given in the "Discussion" section.

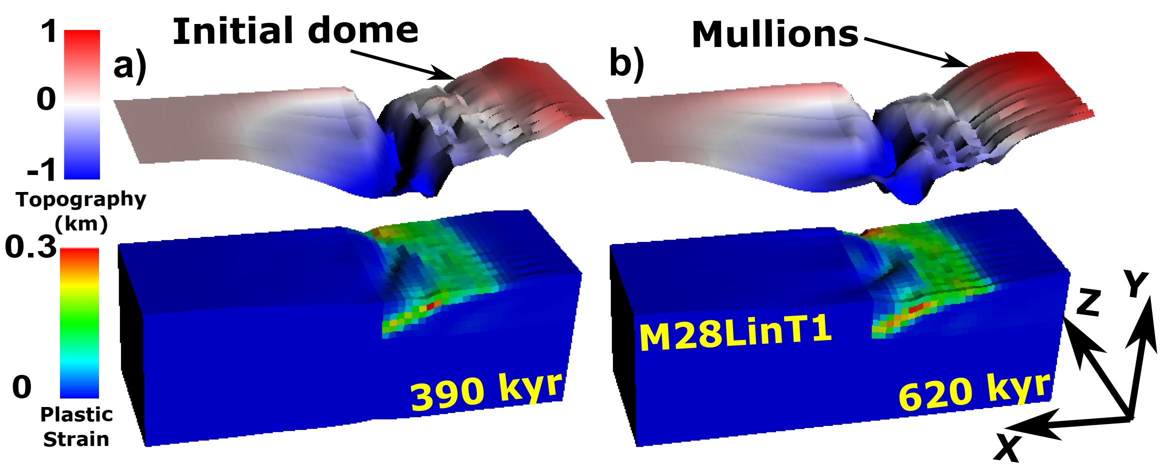

Figure 22: Evolution of mullion structures.

Mullion structures

Mullion structures observed in the models are formed by the along-ridge variation in the location of the termination due to the evolution of faulting. They usually appear at where the termination is closer to the ridge axis. The shape of the footwall follows the trace of the termination as it is exhumed to the surface. At where the termination is bent inward to the ridge axis, an "initial dome" (Figure 22.a) is produced once the hanging wall is exhumed to the seafloor. The wavelength of the mullion structure is determined by the shape of the termination. If the pattern of the termination lasts for a long time and the footwall of the detachment fault keeps being exhumed to the surface following the trace of the detachment fault termination, a mullion structure is produced (Figure 22.b).

3.3 Effects of the functional forms of M variation

3.3.1 Models with M between 0.2 and 0.8 and Type 1 weakening

Major differences among models with M between 0.2 and 0.8 (M28) and Type 1 (T1) weakening lie in the model behaviors in terms of the inward fault jump, the mass wasting and the hourglass-shaped median valley. None of the three models show fault alternation.

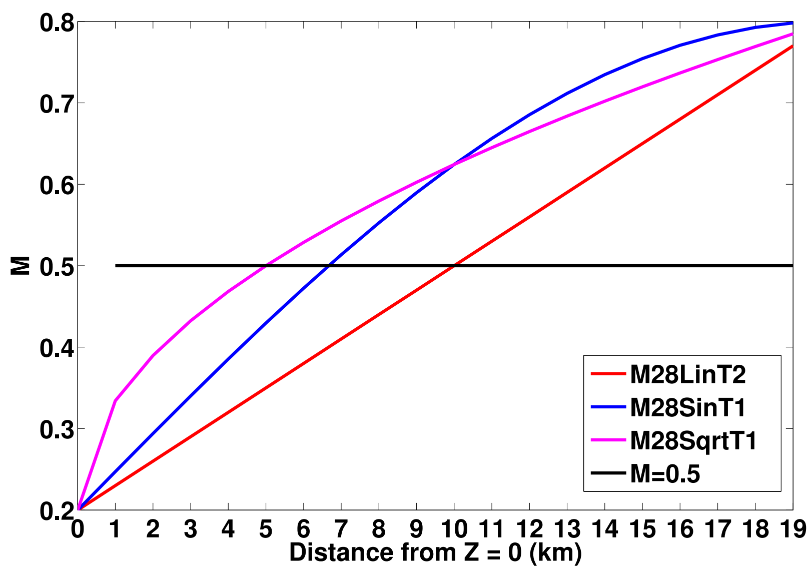

Figure 23: Three functional forms of M variation. M begins to exceed the M = 0.5 black line at Z=10 km, 7 km, 5 km for M28LinT1, M28SinT1 and M28SqrtT1 respectively.

Inward fault jump

Only the models with linear and sinusoidal M variations show inward fault jumps. No inward fault jump occurs when M varies with square root of the along-ridge distance. The termination of a detachment fault retreats towards the ridge axis after a mass wasting and the detachment fault is maintained near the ridge axis.

Timing of inward jumps and the along-strike dimension of the new faults are different between linear and sinusoidal models. The inward jump at the higher M side creates a new fault that accommodates most of the extension at ∼900 kyr and replaces the initial detachment fault (Figure 24, Figure 8.f). The first inward fault jump occurs earlier in a sinusoidal model (e.g., at ∼550 kyr in MXXSinXX)than in the linear reference model. Also, the along-strike length of the new fault in the sinusoidal model is ∼14 km (Figure 24). The timing difference between the linear and sinusoidal models is because M28SinT1 consistently has a higher M values than the M28LinT1 (Figure 23), which results in that the initial detachment fault at the higher M side (M $>$ 0.5) of M28SinT1 is pushed off axis faster than M28LinT1 and thus forming an earlier inward fault jump. The length difference is because M28SinT1 has a greater length along the ridge axis of M $\geq$ 0.5 (Figure 23).

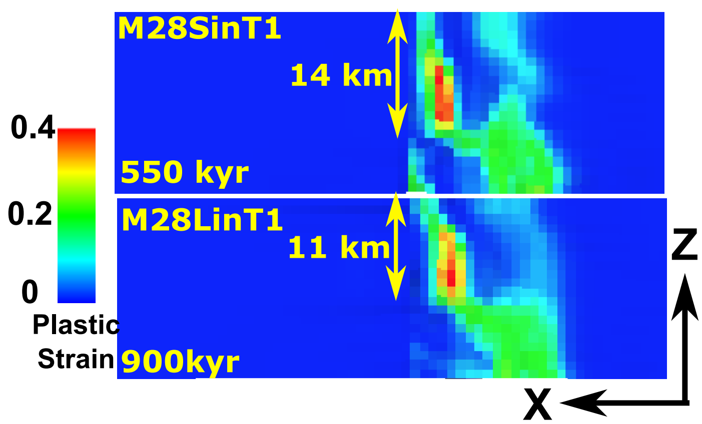

Figure 24: Bird's-eye view for comparing the length and timing of inward fault jump.

Mass wasting

Mass wasting occurs only in the square root model among thoe group of M28 and T1. Qualitatively, it is because the square root profile of M variation has a much higher value of $\frac{\partial M}{\partial Z}$ at the lower M side (Figure 25), which implies a larger along-ridge shear stress σ_{xz} as well as a larger difference in σ_{xy} along the ridge that result in the decoupling between

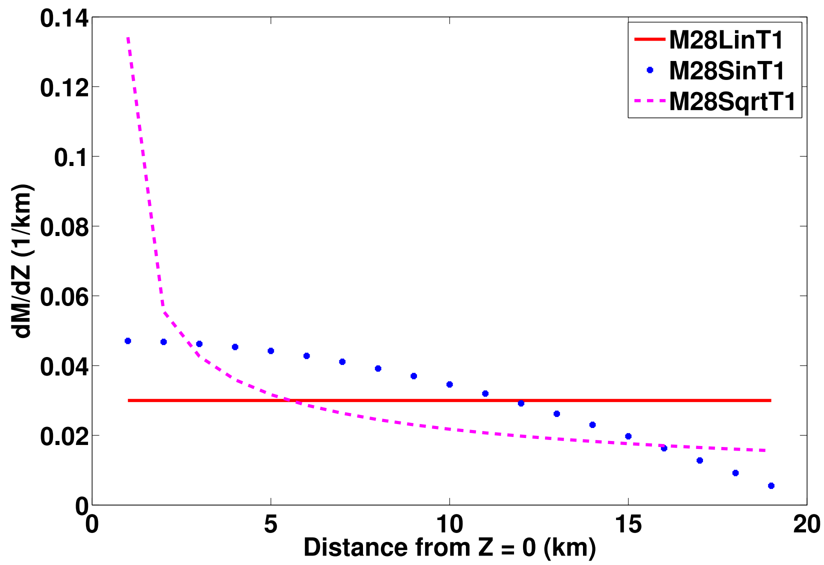

Figure 25: $\partial M/\partial Z$ comparision.

the higher and lower M sides hanging walls.[EC:] [can't understand the last sentence.]

Hourglass-shaped median valley

As shown in Figure 26, differences among the three models are identified. At 160 kyr, the median valley in the model M28SinT1 has [EC:]the smallest cross-sectional (x-y) area [You can't call it a cross-sectional area. Maybe a map-view area? Or just width? And I don't see if it's really the smallest in M28SinT1.] at the higher M side. [EC:]While [You can't use while this way. Please look up the usage of this word.] At the lower M side, the square root model has the smallest area of the cross-section. This is because the [EC:]~~cross-section area inside~~width of the median valley is inversely proportional to the local M value along the ridge. Moreover, the [EC:]breakaways [Mark these on the figure.] at the lowest M value in the linear and sinusoidal models becomes parallel to the ridge axis while the breakaway of the square root model maintains the oblique trend. [EC:]In addition, M28SinT1 has a trough inside the median valley with the highest curvature. [I can't see this. Can you mark this on the figure?] At 500 kyr, M28SinT1 has [EC:]the narrowest median valley [Still can't agree.] at the higher M side and the high topography zone

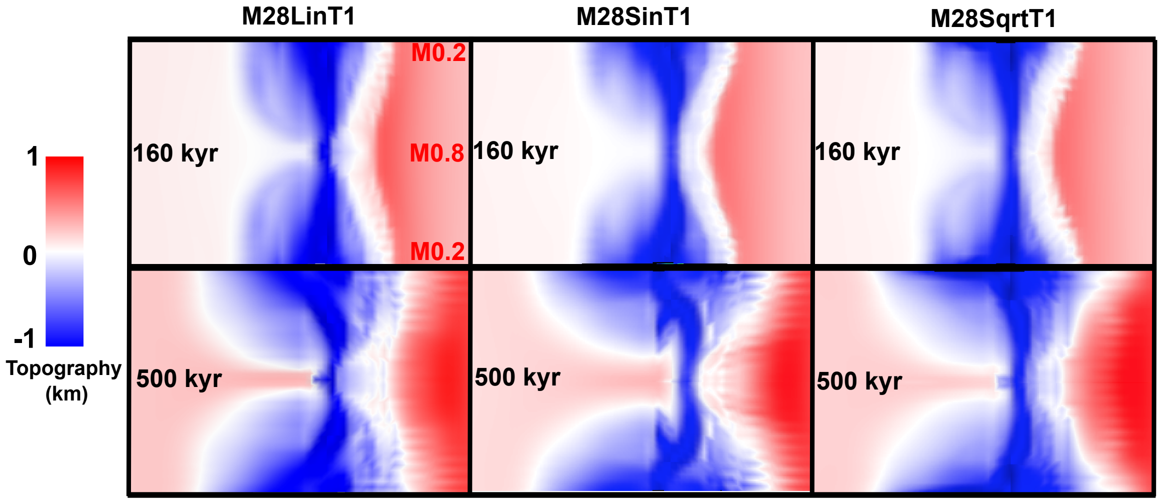

Figure 26: Bird's eye view of the topograpy. EC:(without vertical exaggeration.) [don't need to say. When you did it, you need to say so.] EC: [Say somewhere that you put the origianl and an mirror iamage together in this figure.]

on the left hand side of the ridge axis is the widest. Integrating the topography at the left hand side of the ridge axis of the three models, M28Sqrt has the largest value of integration since it has the largest integration of M along the ridge axis EC: [Did you actually do the integration? Integrating over what? Why integration? Why the largest integration of M means the greatest integration of topography?].

3.4 Effects of the weakening rate

Among the eleven 3D models, three pairs of models have the same parameters but differ only in the weakening rate: M57SinT1/T2, M58SinT1/T2 and M58SqrtT1/T2. I compare them pairwise to single out the effects of the weakening rate on the model behaviors.

Initially, both M57SinT1 and M57SinT2 develop normal faults on both sides of the ridge axis at the lower M side. However, the faults complete propagation towards the higher M side earlier in the fast-weakening model (M57SinT1) than in the slow-weakening model (M57SinT2). In M57SinT1, a mass wasting event occurs at ∼260 kyr but the initial fault remains active without experiencing an inward fault jump (Figure 27.a and b).

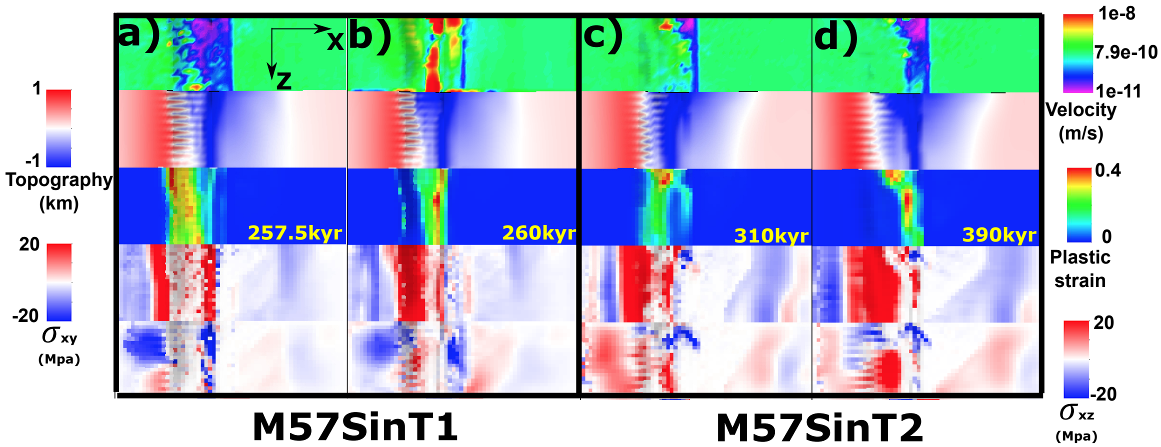

Figure 27: M57SinT2 versus M57SinT1 (Table 1)

In contrast, the slower-weakening model experiences an inward fault jump at the higher M side (M > $^{EC:}$0.55 [Since the range is 0.5-0.7, isn't this value on the lower M side?]) but the initial fault remains active in the M < 0.55 region (Figure 27.c and d).$^{EC:}$ [Without further annotations on the figure, referring to the figure wouldn't help much.] The width of the ''median valley at the lower M side is wider in M57SinT2 than in M57SinT1 (Figure 27.c, d versus a, b)$^{EC:}$ [Again, the figure doesn't help much because one wouldn't know where to look to visually measure the width.]The amplitude of the corrugations of the faster-weakening model (M57SinT1) is greater because the faster weakening rate allows a faster decrease in the cohesion and the lowered cohesion promotes tensile failure in the isochron-parallel direction, which produces the corrugations.

The pairs, M58SinT1/T2 and M58SqrtT1/T2, show a consistent difference that the fault alternation occurs only in the slow weakening models.

3.5 Effects of the range of M variation

Generally, M57 and M58 models create a median valley much narrower and shallower than that of M28 models. Although the difference betweent the M ranages, 0.5-0.7 and 0.5-0.8, is seemingly small, the behaviors of M57 models and M58 ones are noticeably different. A major difference between M57SinT1 and M58SinT1 is that the model with

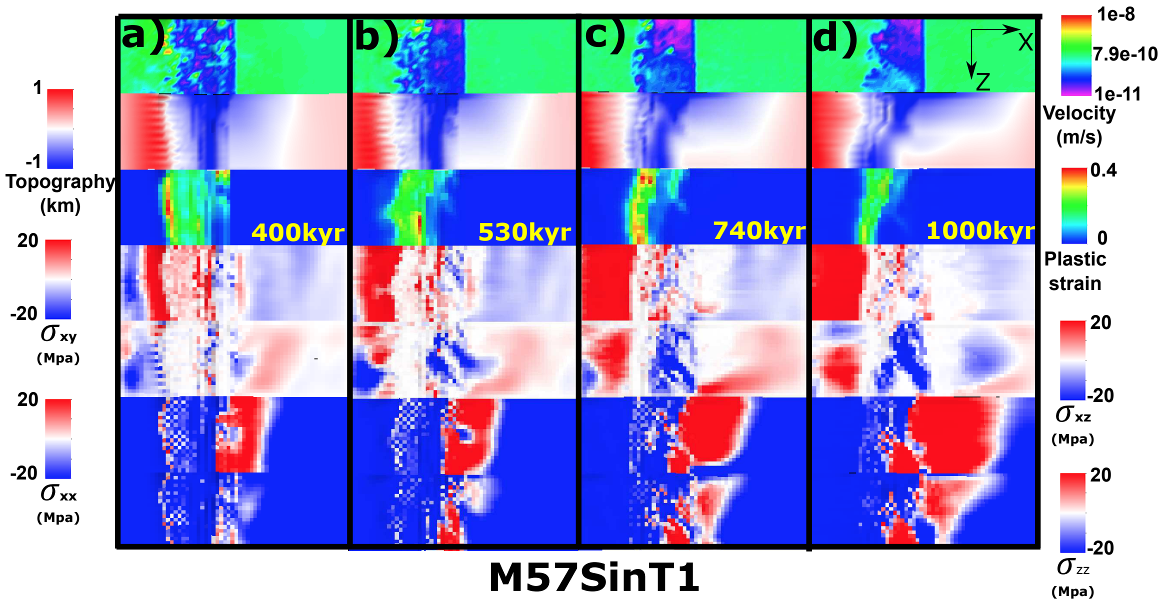

Figure 28: Faulting and stress evolution for M57SinT1.

a greater M range (M58) shows a higher frequency of inward fault jumps, mass wasting events and connection of the offset fault zones. Also, the greater M range appears to promote the fault alternation when combined with a nonlinear M profile and a slow weakening (T2): Only the models M58SinT2 and M58SqrtT2, exhibit fault alternation.

4 Discussion

4.1 Overview of model behaviors

Model results show systematic changes with the average M value ($\bar{M}$), which is the integration of M along the ridge divided by the ridge length. $\bar{M}$ values of all the models are listed in Table 3. $\bar{M}_{M58} > \bar{M}_{M57} > \bar{M}_{M28}$ and within each M range, $\bar{M}$ for functional form with sqaure root is higher than that for the sinusoidal form, which in turn is higher than the linear form.

Table 3: Average M values of the models.$^{EC:}$~~20 km segment. (The value is calculated by integrating M along the ridge axis and divided by the length of the model domain in z-axis.)~~

Function \ M range	M28	M57	M58
Linear	0.4850	0.5950	0.6425
Sinusoidal	0.5668	0.6223	0.6834
Square root	0.5837	0.6279	0.6918

To facilitate the challenging task of describing the complicated behaviors of each model as well as comparing different models, I visualize the model behavior as in Fig. 29. Each plot has the amount of extension in km as the horizontal axis and M values as the vertical axis. The plot can succinctly show what structure appears, how long it takes to be created or remains active, and where it is created along the ridge. For instance, from the plot for M57SinT1 ($\bar{M} = 0.6223$) in Fig. 29, one can see that an antithetic fault first shows up after about 17 km of extension on the low M end, a mass wasting event occurs after about 13 km of extension and the inward fault jump is absent in this model. Similarly, the plot for the M57SqrtT1 model ($\bar{M} = 0.6279$) clearly shows that this model experiences two inward fault jumps.

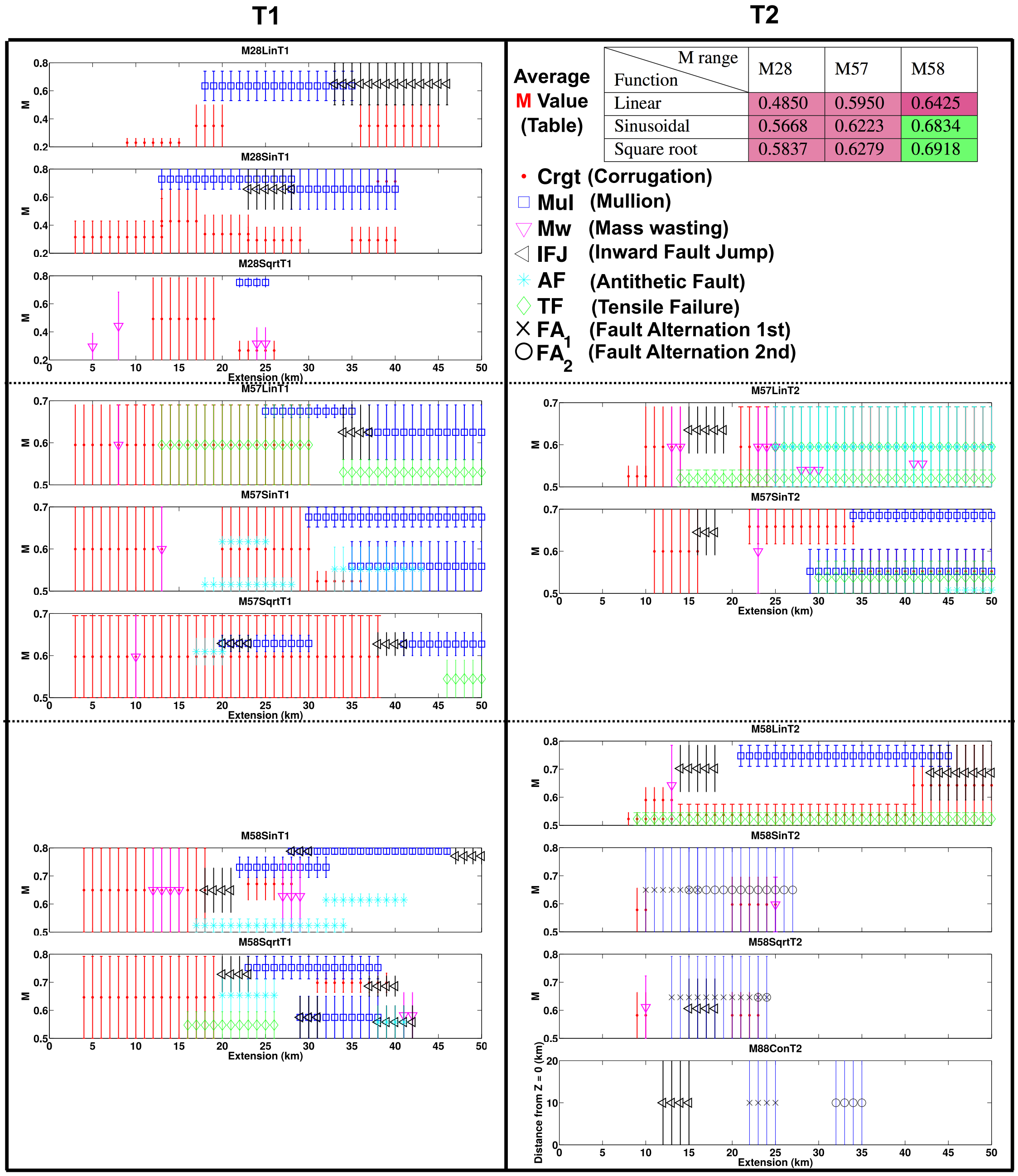

Figure 29: Initiation and duration of main structural features.[EC:] [Labels of an individual plot are too small. Symbols can be bigger, too. You probably want to remove the table from this figure and keep it as a stand-alone table as I tried.]

Models with the Type 1 weakening, which is slower then Type 2, on the left column of Figure 29, show that they show more complex and dynamic behaviors as $\bar{M}$ increases. In other words, more of the main structural characteristics are created and they tend to have a higher recurrence frequency as $\bar{M}$ increases. For instance, the inward fault jump occurs earlier and lasts a shorter period of time in M28SinT1 than in M28LinT1, the former of which has a higher $\bar{M}$. Furthermore, mass wasting events occur only in M28SqrtT1, the model with the highest $\bar{M}$ among these M28 and T1 models. The trend of greater complexity for higher $\bar{M}$ continues in the group of M57-T1 models. Corrugations are created earlier along the whole 20 km ridge segment than in the M28-T1 models. Unlike the M28-T1 group, all three models in the M57-T1 group have mass wasting. The two M58 models have 3 or 4 inward fault jumps but the M57 models have at most two of them. Also, corrugations are created earlier in the M57 models than in the M58 ones, which suggests that corrugation favors a specific range of $\frac{\partial M}{\partial Z}$, not necessarily higher $\bar{M}$. Between M58SinT1 ($\bar{M} = 0.6834$) and M58SqrtT1 ($\bar{M} = 0.6918$), the major difference is M28SqrtT1 has twice inward fault jumps at the lower M side because M values are higher at the lower M side.

When comparing models with different weakening rates, the most obvious difference is that only two of type 2 models with $\bar{M} > 0.6425$ (i.e., M58SinT2 and M58SqrtT2) generates alternating faults [EC:] [This fact seems stated too many times here and there.]. The models that exhibit the fault alternation [EC:] ~~don't~~do not create the mullion structure because the high frequency of fault alternation allows the pattern of termination required for the mullion structure to last only for a short period of time. M58LinT2 ($\bar{M} = 0.6425$) does not show the fault alternation, which suggests that not only the range of M (M58) but also the average M value along the ridge $\bar{M}$ are responsible for the fault alternation. This provides an upper limit of $\bar{M} = 0.6425$ in our 3D models for producing long lasting detachment faults that can generate OCCs. Comparing M57T2 and M57T1 models show that M57T2 models generally have earlier inward fault jumps but later corrugations. For the model with constant M = 0.8 along the ridge axis, the inward fault jump and fault alternations have a period of ∼10 km of extension which is consistent with that of field observations. Corrugation, mullion structures, mass wasting, antithetic fault and tensile failure are not produced in constant M model M88ConT2 and it implies that varying M is necessary for producing those features.

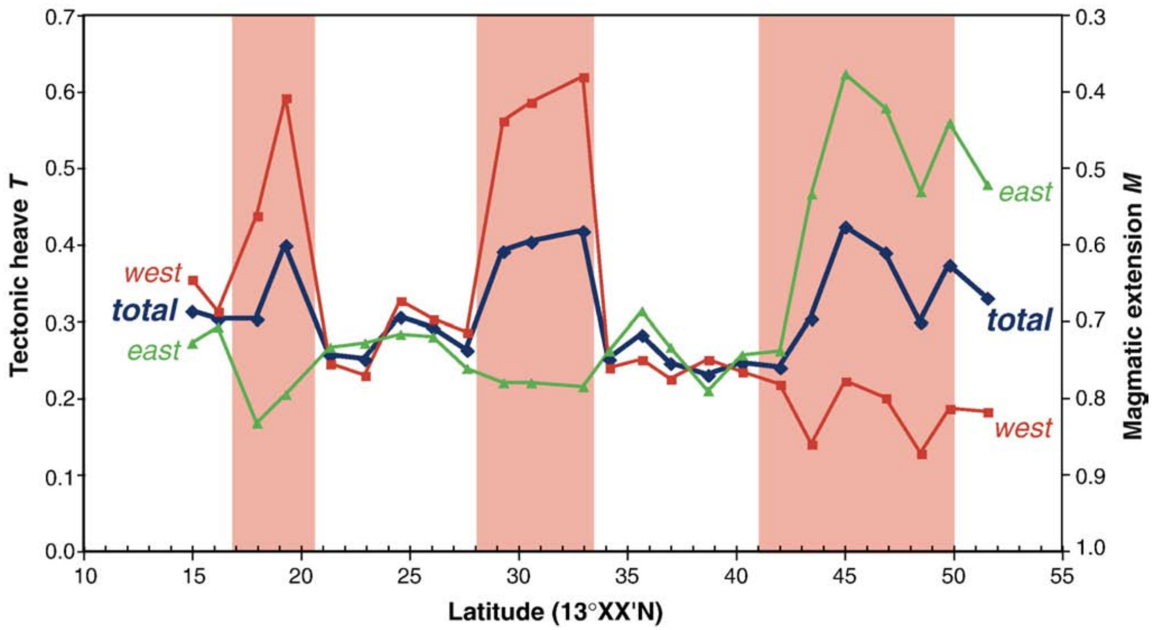

Figure 30: Along-axis variations in total accumulated tectonic heave T in the past 1.86 Ma (since chron C2n), and consequent inferred magmatic component M (= $1 - $T) as a proportion of total plate separation (blue line). Pink shaded areas delineate loci of the active or recently active OCCs. The relative contributions of tectonic strain from the western and eastern flanks of the axis that give rise to the total heave T are shown by red and green lines respectively. Adapted from [MacLeod et al., 2009].

In addition, the upper limit of $\bar{M} = 0.6425$ for allowing a long lasting detachment fault to produce an OCC in our model is consistent to the results from a near-bottom sidescan bathymetric profiler survey and sampling study of the Mid-Atlantic Ridge near 13 °N [MacLeod et al., 2009]. As shown in Figrure 30, the average M value $\bar{M} = 0.63 \pm 0.05$ for the pink area where OCCs are present while when there is no OCC, $\bar{M} = 0.73 \pm 0.03$.

Under similar physical conditions of our model setup (e.g. thermal structure, rheology relationship, spreading velocity, weakening rate), the upper limit of $\bar{M} = 0.6425$ predicts a boundary value between two observed morphological end members for slow spreading ridges: 1) long wavelength OCCs generated by a detachment fault; 2) high frequency abyssal hills results from symmetrical spreading of alternating high angle normal faults. Although the number of $\bar{M} = 0.6425$ is highly consistent with natural observation (e.g. [MacLeod et al., 2009]), we still need more works for a comprehensive result because model parameter such as viscosity of the underlying asthenosphere also contributes to whether fault alternates. For example, [Allken et al., 2012] shows that higher value of viscosity of the ductile asthenosphere leads to better coupling between crust and mantle and promotes distributed muliple faulting rather than a focused long-lived detachment fault.

Previous 2D studies suggest that OCCs are most likely to form when M = 0.3 $\sim$ 0.5 [Buck et al., 2005;Tucholke et al., 2008]. However, conflicts exist between model prediction and nature observation in both the upper and lower limits. For the upper limit conflict that OCCs are observed with M $>$ 0.5, Olive et al. [2010] suggests an explanation from a 2D model study that magma supplied in the ductile lower crust and upper mantle will not affect the faulting pattern and thus allows OCCs to be created under excessive diking. However, our 3D model results provides an alternative explanation that due to the along ridge coupling (i.e. torsion and shear), the region (M = 0.3 $\sim$ 0.5) along the ridge that promotes stable spreading by detachment faulting helps maintain the normal fault outside the region along the ridge. Once the detachment fault initiates along the whole ridge segment, it is very hard to modify the faulting pattern especially for a faster weakening rate (type 1). Thus, the detachemnt fault at the higher M side (M $>$ 0.5) can still last for more than 20 km of plates separation (Figure 29.M28LinT1) before the fault alternation or inward fault jump ceases the exhuming process of the ultramafic mantle rocks. This along ridge coupling can also explain the conflict at the lower limit end when OCC is produce with observed M $<$ 0.3 (e.g., Dick et al., 2008; Grimes et al., 2008; Baines et al., 2008). Our 3D result suggests an extended range of M for OCCs formation than previous 2D studies (M = 0.3 $\sim$ 0.5) [Buck et al., 2005;Tucholke et al., 2008].

4.2 Comparing model results with natural observations

4.2.1 Inward fault jump

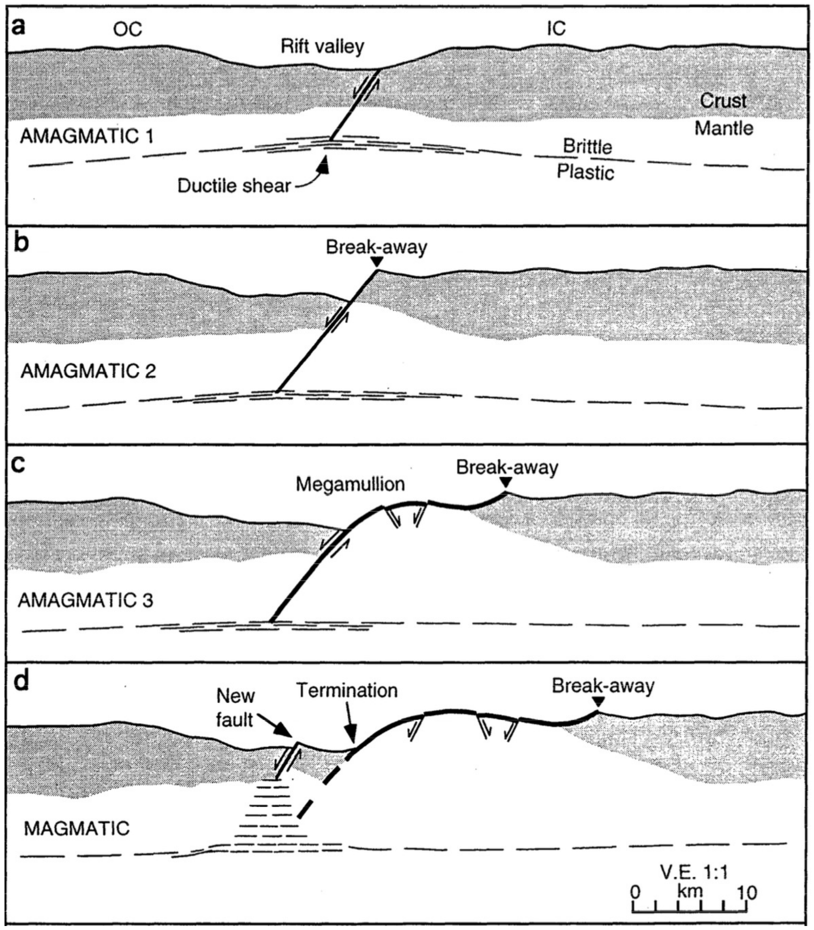

Figure 31: Schematic development of a megamullion. No vertical exaggeration. (a)∼(c) shows the detachment fault evolution during amagmatic phase. (d) Increased magma supply pushed the detachment fault away from ridge axis and forms a new normal fault near the ridge axis ("inward fault jump"). Adapted from [Tucholke et al., 1998].

The term "inward fault jump" is first suggested in a study of geological and geophysical data from the Mid-Atlantic Ridge [Tucholke et al., 1998]. It is the end phase of a general evolution of an OCC as is illustrated in Figure 31. In the begining of a long amagmatic phase (Figure 31.a∼c) of seafloor spreading, a high angle normal fault cuts throught the brittle lithosphere and roots in the brittle-ductile transition (BDT) (Figure 31.a). When the fault keeps slipping, the breakaway moves off axis and the fault begin to rotate to a lower dip angle (Figure 31.b). Then, the exposed fault surface roll over and as the detachment fault keeps exhuming lower crust and upper mantle rocks, it generates a dome shape megamullion (OCC). The high angle normal faults cut the detachment fault surface where it is exposed to the seafloor is probably caused by the bending stresses during footwall roll over (Figure 31.c). Then, when magma supply at the ridge center increases and pushes the detachment fault away from the ridge axis, the OCC formation is terminated by the new fault near the ridge axis which is termed as the "inward fault jump". As shown in the figure, initially, the footwall of this new fault is mostly composed of crust material like basalt, however, if this new fault can last a long period of time, it can also exhume lower ultramafic material.

In our model, *EC:* most of the inward fault jumps last [What do you mean by the jumps "last"? Doesn't a jump imply that it's an event rather than a process. Only for the latter, it would make sense to talk about a lasting period.] less than 5 km of plates extension before the mantle materials can be exhumed to the seafloor. However, the M28LinT1 model produces an inward fault jump lasts for ∼15 km of extension (Figure 29.M28LinT1) and produces a dome-shaped OCC ajacent to the initial one further way from the ridge axis (Figure 8.h). This behavior might explain the formation mechanism of the brother Abel and Cain domes of the Kane megamullion at 23 °N MAR. As shown in Figure 32, our model behaviors are consistent with the nature observation in terms of the breakaway and the wavelength of the domes assuming M decreases form south to north along the ridge axis. First of all, the breakway of the detachment fault is further away from the ridge axis at the northern than the sourthern end. Second, the Abel and Cain domes are larger than the Adam and Eve domes because the inward fault jump lasts longer at where M is relatively lower.

A seismic study [Xu et al., 2009] showed that the Kane OCC is terminated at around 2.1 Myr ago when an eastward fault jump occured, i.e. when a new normal fault formed

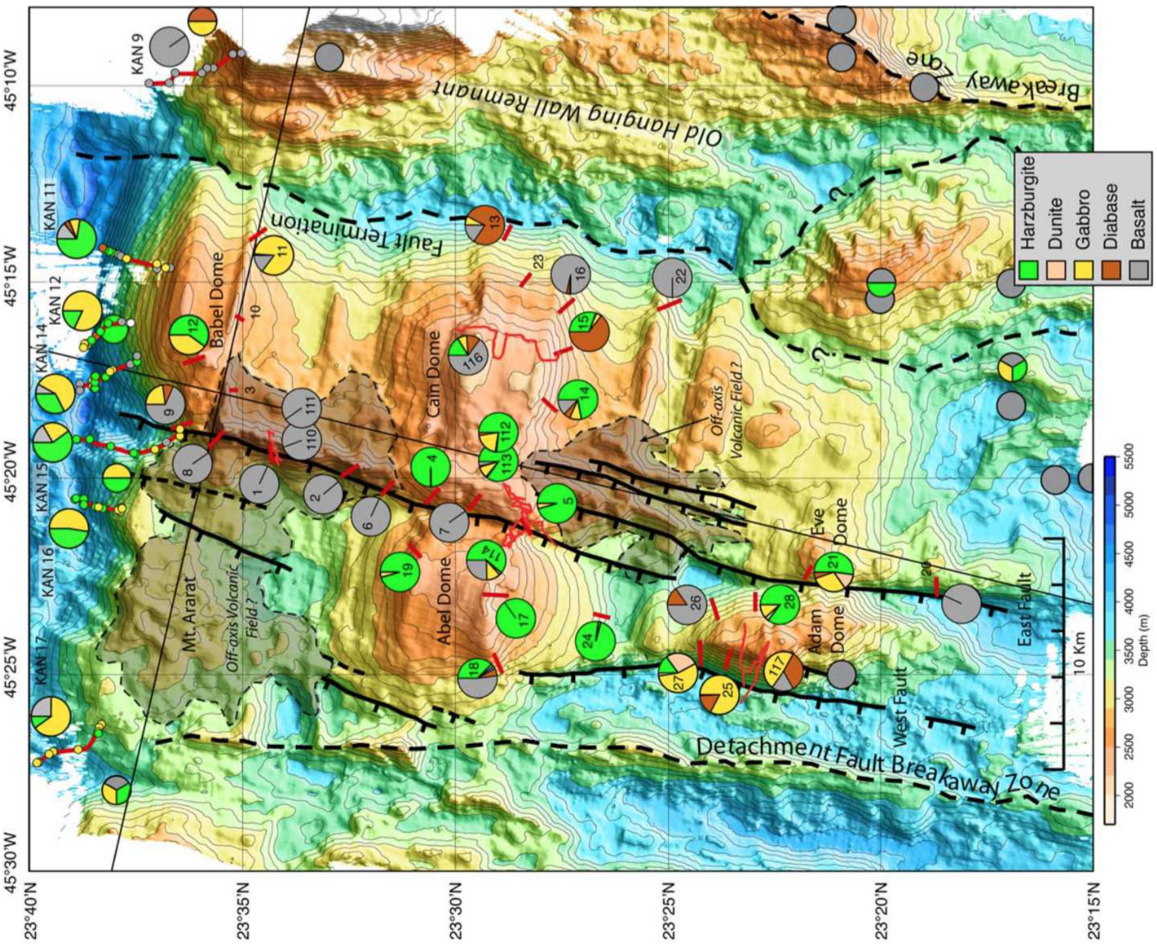

Figure 32: [EC:] [Still should say what is being shown.] Adapted from [Dick et al., 2008].

in the rift valley and captured a segment of the basaltic hanging wall. The velocity structure from their P wave tomography study verifies that the hanging wall block eastern to the Cain dome has a lower velocity corresponds to basaltic rocks (Figure 33).

4.2.2 Fault alternation

For slow-to-intermediate spreading ridges, the off-axis morphologies have two endmembers. One is the high-frequency abyssal hills that are relatively symmetric across the ridge axis. They are usually found closer to the ridge segment center (crossection A-A′ in Figure 34). The other is the long wavelength asymmetrically spreading OCCs (crossection B-B′ in Figure 34). [EC:] [looks like you can refer to Fig. 2. What extra information does this

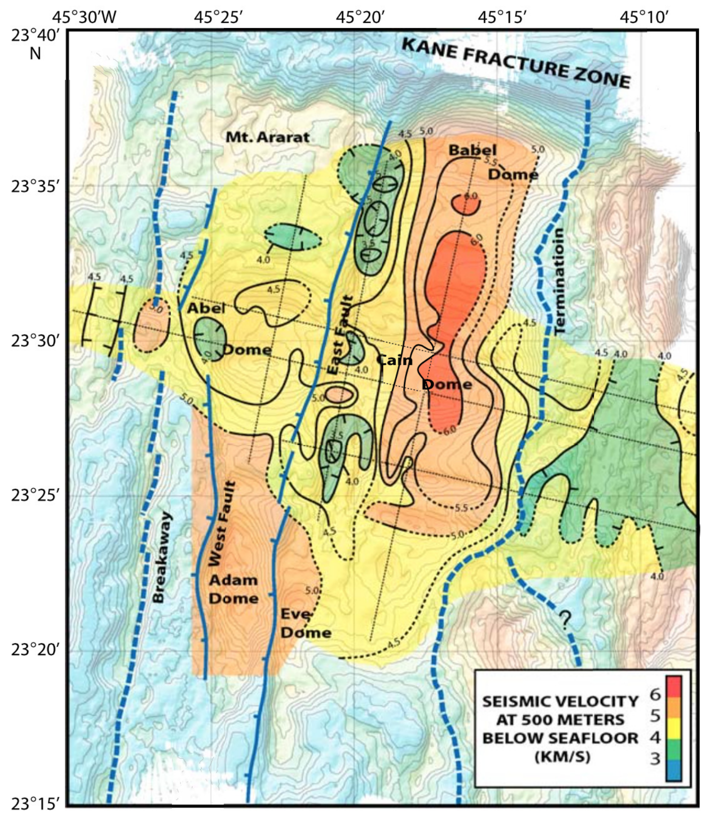

Figure 33: [EC:] [Still should say what is being shown.] Adapted from [Xu et al., 2009].

new figure provide? Also, it is not clear at all that A-A' is at the segment center and B-B' is at the segment tip.] What is the mechanism for this distinct difference along the ridge? [EC:] [Didn't Buck et al. (2005) and/or Tucholke et al. (2008) already presented this view?] The fault alternation behavior in our model provides a 3D perspective for answering the question. When average M $\bar{M}$ is higher than 0.6425 with slower weakening rate (type 2), high frequency abyssal hills are generated. For example, M88ConT2 produces abyssal hills with ~10 km in wavelength due to fault alternation (Figure 29.M88ConT2) [XT:] add the hyperref of the figure of ConM88T2 here. Note that the wavelength of the abysall hills in our models is consistent with the nature observation as marked in Figure 34.

The parameters that controls fault alternation have been proposed by Lavier et al. [2000]. Lavier et al. [2000] focused on the trade-off between bending forces (ΔF_b) as a function of fault offset ΔX and force change due to strain weakening (ΔF_w) that is also a function of ΔX. They showed that the strength weakening on the existing fault combined

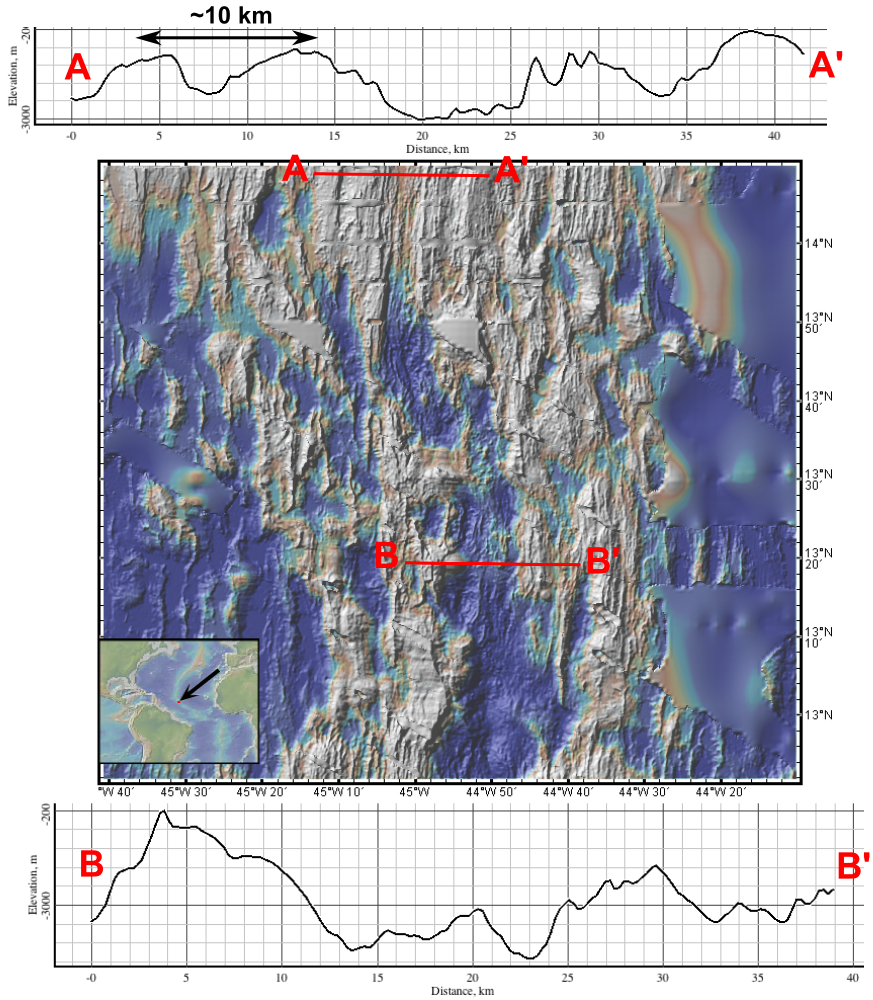

Figure 34: Bathymethry from 12.8∼14.2 °N Mid-Atlantic Ridge. Crossection A∼A′ and B∼B′ are 5 times vertical exagerated. From GeoMapApp.

with bending force resists further offset of the fault plays a major role in determining the stress state at the regions other than the active fault. Their analysis explains how higher [EC:] characteristic fault offset [Did you explain what this is already?] (ΔX_c) or slower strain weakening results in multiple faults rather than only one fault lasting. As ΔX increases on a fault at a spreading center, the change in bending force ΔF_b increases and the strength at the fault interface decreases due to weakenging ΔF_w (Figure 35). If the net force change $\Delta F = \Delta F_b + \Delta F_w$ is positive, it means that it is getting harder and harder to maintain the existing fault and stress will begin to accummulate at the other areas which eventually break another fault. ΔF_b initially increases fast with respect to ΔX and then

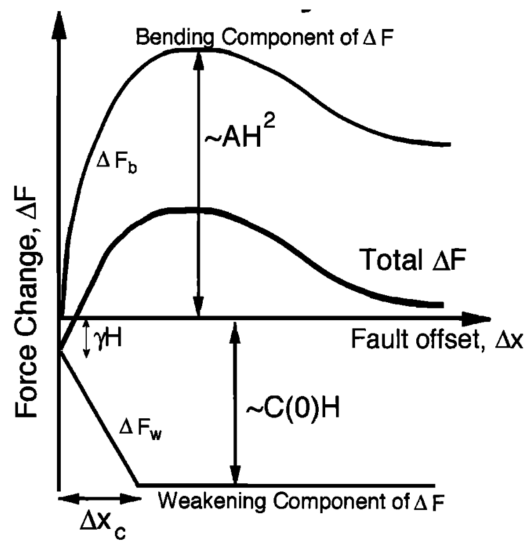

Figure 35: Trade-off between change in bending force ΔF_b and weakening in the fault interface ΔF_w. H is the thickness of the brittle crust and γ is the size of initial weak perturbation and A defines the maximum bending force change. Adapted from [Lavier et al., 2000]. (For more details, please refer to [Lavier et al., 2000])

when the detachment fault surface roll over, ΔF_b reaches its peak value and begins to decrease a little and maintains at a constant value. If the strain weakenging is fast enough that the net effect force ΔF is always negative, then most of the stress will be released by the existing fault and thus no conjugate or multiple faults will be generated. Our model results are consistent with this analysis in that only [EC:]Type 2 [we need to keep reminding readers of what Type 2 weakening is. This is why I suggested to use a more explicit naming. If you want, we can rename Type 1 and Type 2 later.] weakening (slower weakening with higher ΔX_c) produces an alternating normal fault on the conjugate plate.

4.2.3 Mass wasting

The mass wasting behavior in M28SqrtT1 model produces a fault scarp of $\sim$1km in relief, 40km in length parallel to the ridge axis. It seems to form when the detachment fault rolls over and induces bending stressses that generate the high angle fault which cuts the weak detachment fault surface and decouples the spreading breakaway and the highly defomed fault hangingwall. However, the temporally sparse model outputs do not capture the mo-

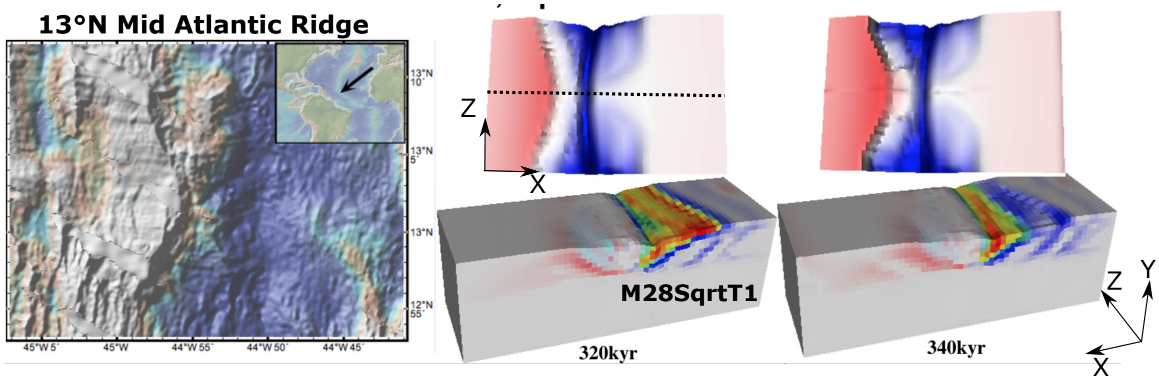

Figure 36: Comparing bathymetry at 13°N Mid-Atlantic Ridge to the mass wasting behavior of M28SqrtT1. The model topography is a mirror symetric flip according to the dash line, it shows the case of M varies in a square root functional form from 0.2 to 0.8 to 0.2. The bathymetry image is generated by GeoMapApp [Ryan et al., 2009].

ment when the even is triggered. The topography at 13°N Mid-Atlantic Ridge also has a fault scarp with very similar curved geometry with ∼1km in relief. However, the 1 km relief might be simply relfecting the model resolution of 1 km so further investigation is necessaray before I can conclude on this coincidence.

4.2.4 Hourglass shape median valley

Due to the variation in diking along the ridge-axis, an hourglass shape of median valley is also produced in the model where the narrowest center corresponds to the region with higher magma supply (M=0.8). An hourglass-shaped median valley is frequently observed in the nature along the slow-to-intermediate spreading ridges like the Mid-Atlantic Ridges [Sempéré et al., 1993], where the waist of the hourglass is usually narrower and shallower. From an analysis of the sea beam bathymetry along the MAR between 24 ° 00 ′N and 30 ° 40 ′N [Sempéré et al., 1993], nine hourglass shape valleys are identified. They share similar dimensional scale (∼40 km × ∼40 km) with our model. For example, there is an hourglass around 22 ° 30 ′ that is 45 km long and 15 km wide (Figure 38). The observed width and depth of the hourglass can be used for inferring which evolution stage the rift valley is in. For instance, the one shown in Figure 38 corresponds to a early stage

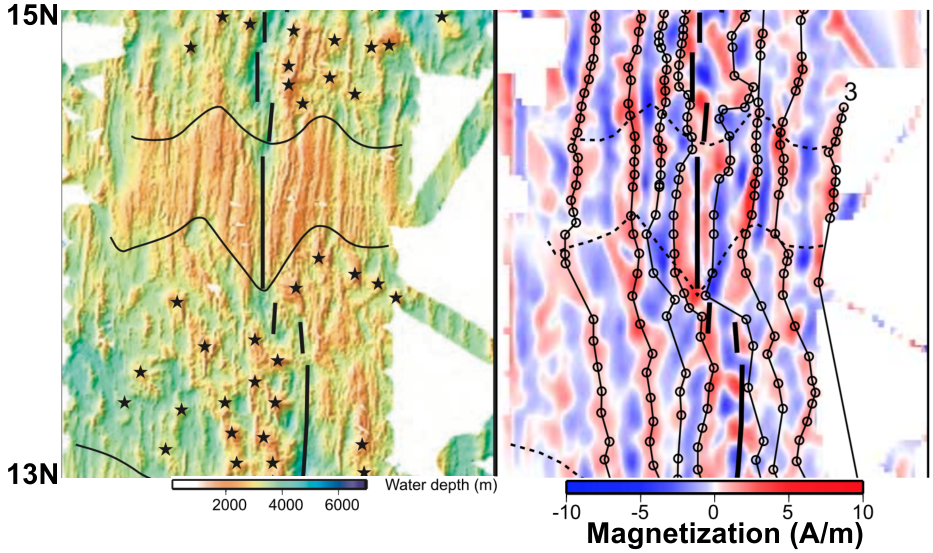

Figure 37: Bathymetry and magnetization of 13∼15 °N MAR. Adapted from [Smith et al., 2008].

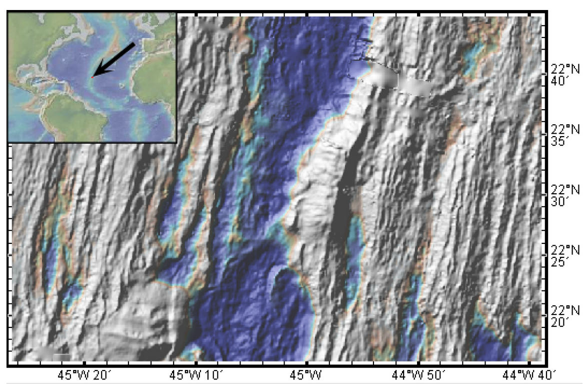

Figure 38: Hourglass median valley at 22 ° 30 ′N MAR. Image is generated from GeoMapApp.

of our model because it has a relative symmetrical and narrow shape XT:add a hyperref figure of model example for this.

4.2.5 Mullion structure

Mullion structures are frequently observed on the surface of OCCs. For instance, the mullion structures on the surface of of the Cain dome has a wavelength of ∼3.5 km as marked in the Figure 39.B∼B′. EC: [Your figure and these texts make me wonder, which is the

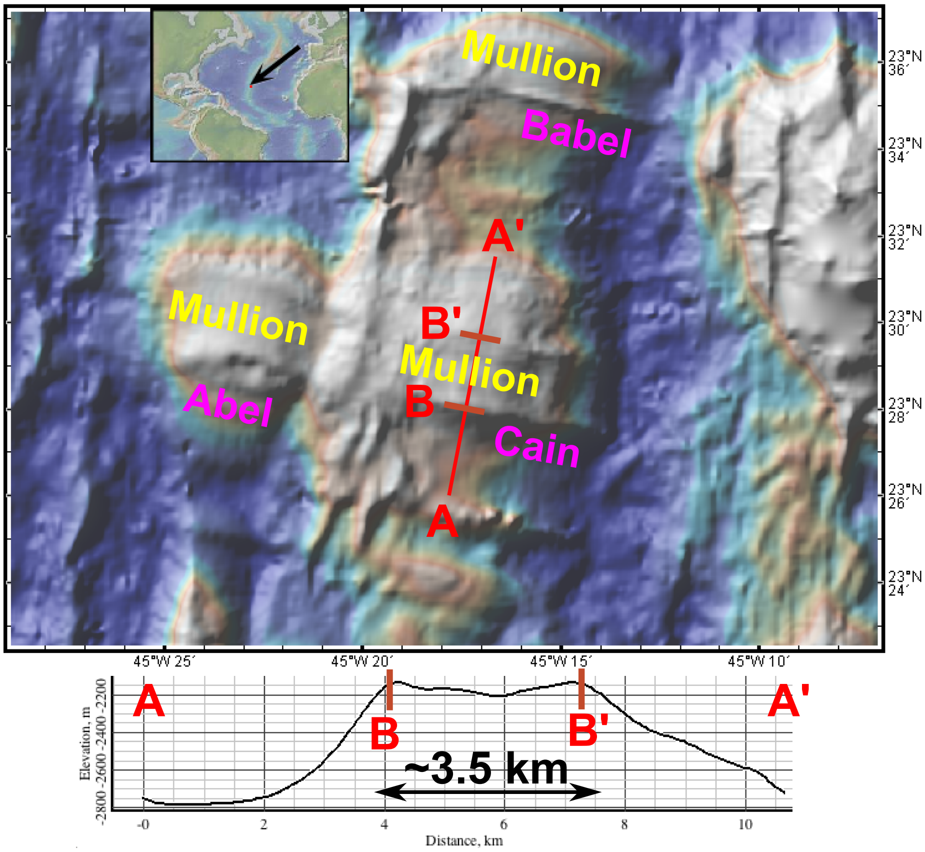

Figure 39: [EC]Mullion structures [No, the figure shows bathymetry map. It is you who interpret it as showing mullion structures. So, it should be like, Bathymetry around the Kane OCC at 23degN MAR. Created with GeoMapApp.] on the surface of Kane OCC at 23 °N MAR. Image is generated from GeoMapApp.

mullion you are talking about the dome itself or the smaller-scale structure marked by B and B'?] The geometry and length scale of these mullion structures bears significan visual similarity with those of our reference model, M28LinT1 (Figure 22). Model results indicate that the mullion structure mostly forms when the termination has a curved shape that can last for a long period of time and the spreading-parallel mullion structure is produced following the shape of the termination. Where the termination is curved toward the ridge axis corresponds to the larger and higher part of the mullion structure. As shown in Figure 32, the spatial distribution of the mullion structure of the Cain dome is consistent with the termination that is [EC]curved inward to the ridge axis [Not clear. Mark on the map.].

4.2.6 Corrugations

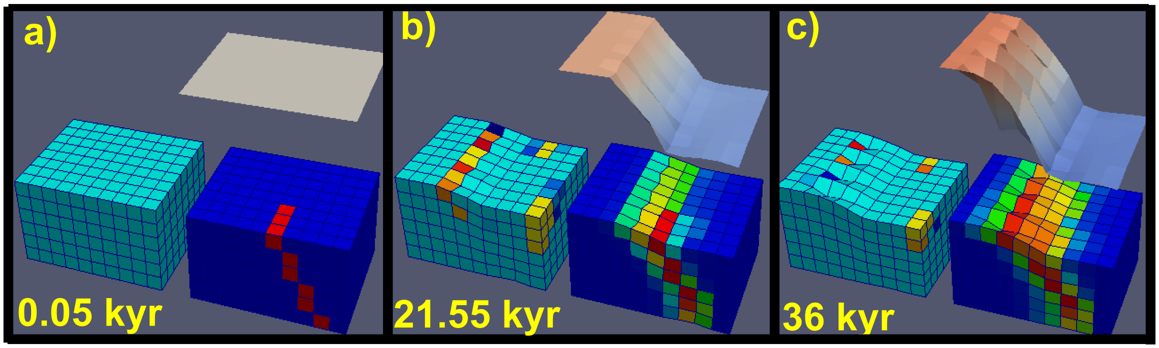

Figure 40: Simpler 3D model with 4 km of seawater pressure on top. Seeds are partially added along the ridge segment. Color scale is the same as Figure 21.

As decribed in the "Results" section, the corrugations are formed due to the moving off axis tensile failure which results from the asynchronous faulting along the ridge. This mechanism is further verified by simpler 3D models.

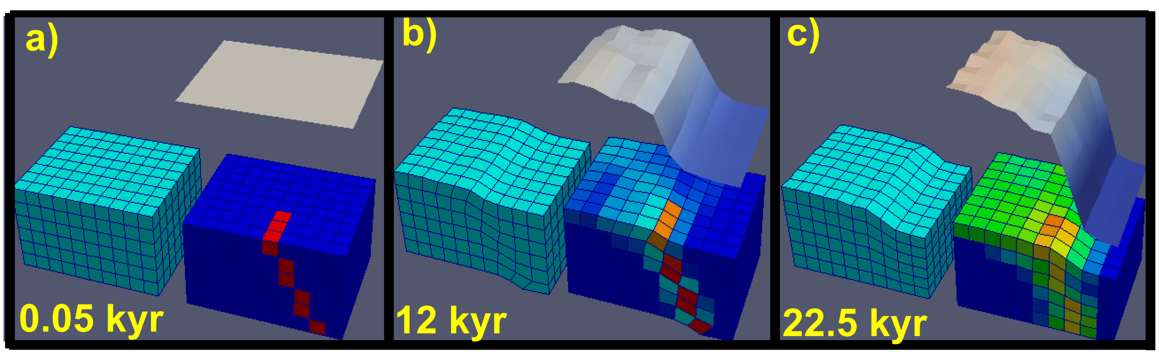

Figure 41: Simpler 3D model with 20 km of seawater pressure on top. Color scale is the same as Figure 21.

When seeds are partially added along the ridge segment for simulating the effects of asynchronous faulting where normal fault initiates earlier at the region with initial seeds, corrugations are produced by the model (Figure 40). However, when 20 km of sea water pressure is added on top of the seafloor to suppress tensile failure, [EC:]no corrugation [corrugation does seem to occur in c)!] is produced (Figure 41). This verifies that the corrugation is related to tensile failure in the fault plane exposed on the surface.

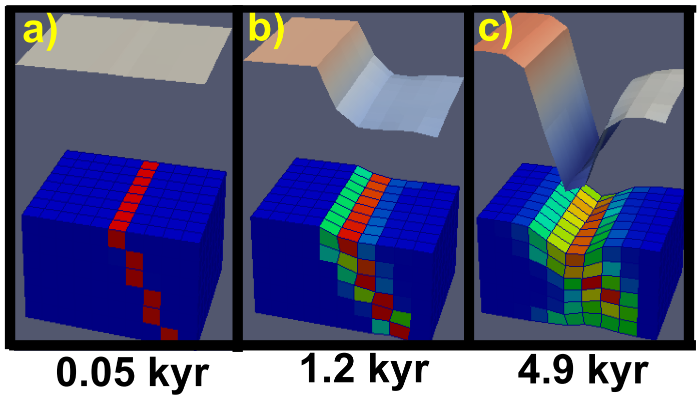

Figure 42: Simpler 3D model with 4 km of seawater pressure on top. Seeds are added along the whole ridge segment. Color scale is the same as Figure 21.

In addition, when seeds are added along the whole ridge segment, which results in synchronous faulting, no corrugation is generated (Figure 42). This verifies that along ridge asynchronous faulting is necessary for creating corrugations.

As mentioned in [Smith et al., 2014], corrugations are observed in many scales from $\sim$10 km wavelength megamullion to $\sim$1 km wavelentgh corrugations or even smaller 10$\sim$100 m striations. On most of the OCC surface, corrugations coexist on a wide range of scales (e.g. MacLeod et al., 2009). However, the formation mechanism is still enigmatic [Smith et al., 2006]. Several hypotheses were proposed. Spencer [1999] suggests the continuous casting model in which the ductile footwall of a detachment fault is continuously exhumed to the surface and is casted by the shape of the cold and strong hanging wall. This hypothesis is consistent with the mullion structure produced in our models. Smith et al. [2014] proposes another hypothesis that pre-existing offsetted faults or weak zones along the ridge break through and connect to each other forming a curved termination that can produce corrugations. This is called the anastomosing behavior (e.g. Ferrill et al., 1999; Wong and Gans, 2008) and is also produced in our models especially when there is inward fault jumps, antithetic faults or tensile failures happen at part of the ridge segment which perturbs the continuity of the termination along the ridge. In addition, Tucholke et al. [1998] mentioned that as oceanic lithosphere moves off axis, horizontal and isochron-parallel extension is expected due to contraction of the cooling lithosphere. Among these hypotheses, I proposed that the asynchronous faulting due to the varying M along the ridge is most likely to be responsible for the relatively uniform $\sim$2 km corrugations. And these corrugations can also be superimposed onto the surfaces of mullion structures or OCCs.

5 Conclusions

To the first time, we model in 3 dimensions on how varying M value (magma supply) along the the mid-ocean ridge segment can control the interaction system between tectonics and magmatism and how is it responsible for the major bathymetric features observed on the seafloor.

Six commonly observed MOR features (i.e. inward fault jump, fault alternation, mass wasting, hourglass median valley, corrugation and mullion structre) are produced by our model. By comparing the model results and local field observations, faulting evolution history as well as spatial and temporal variation of magma supply can be inferred.

Three controlling parameters are investigated. They are three ranges of M (i.e. M28, M57 and M58); three type of functional forms of M variation (i.e. linear, sinusoidal and sqaure root) as well as two types of weakening rates (i.e. faster type 1 and slower type 2). As result shows, besides many different structural features generated by different functional forms and ranges of M variations along the ridge, the average M value ($\bar{M}$) along the whole ridge segment is the major value that is responsible for the two end members of off-axis morphologies, i.e. when $\bar{M} > 0.6425$ with type 2 weakening, the model generates symmetrial spreading, high frequency abyssal hills while when $\bar{M} <= 0.6425$, fault tends to rotate to a low angle, long lasting detachment fault that can exhume ultramafic rocks to the seafloor producing a domal OCC. Also, our 3D model results resolve the discrepancy between previous 2D model studies and field observations that model studies suggest OCC is produced with M values between 0.3 to 0.5 while field observation reveals cases of OCC forming with observed M beyond both lower and upper limits. Base on this thesis study, we propose a new perspective for explaining cases when OCC forms with local M value is lower than 0.3 or larger than 0.5 by the along ridge coupling argument.

In addition, we propose a new hypothesis of the asynchronous faulting induced tensile failure as one possible formation mechanism for the enigmatic corrugations widely observed on the surface of OCCs.

Bibliography

V. Allken, R. S. Huismans, and C. Thieulot. Factors controlling the mode of rift interaction in brittle-ductile coupled systems: A 3d numerical study. *Geochemistry, Geophysics, Geosystems*, 13(5):1–18, 2012. ISSN 15252027. doi: 10.1029/2012GC004077.

G. Baines, M. J. Cheadle, B. E. John, and J. J. Schwartz. The rate of oceanic detachment faulting at atlantis bank, sw indian ridge. *Earth and Planetary Science Letters*, 273 (1-2):105–114, Aug. 2008. ISSN 0012821X. doi: 10.1016/j.epsl.2008.06.013.

M. Behn, W. Buck, and I. Sacks. Topographic controls on dike injection in volcanic rift zones. *Earth and Planetary Science Letters*, 246(3-4):188–196, June 2006. doi: 10.1016/j.epsl.2006.04.005.

M. D. Behn and G. Ito. Magmatic and tectonic extension at mid-ocean ridges: 1. controls on fault characteristics. *Geochemistry, Geophysics, Geosystems*, 9(8):n/a–n/a, Aug. 2008. ISSN 15252027. doi: 10.1029/2008GC001965.

D. Blackman, J. Karson, and D. Kelley. Geology of the atlantis massif (mid-atlantic ridge, 30 n): Implications for the evolution of an ultramafic oceanic core complex. *Marine Geophysical* . . . , 2002.

R. Buck, L. Lavier, and A. Poliakov. Modes of faulting at mid-ocean ridges. *Nature*, 434 (7034):719–23, 2005. ISSN 1476-4687. doi: 10.1038/nature03358.

J. P. Canales, B. E. Tucholke, M. Xu, J. a. Collins, and D. L. DuBois. Seismic evidence for large-scale compositional heterogeneity of oceanic core complexes. *Geochemistry, Geophysics, Geosystems*, 9(8):n/a–n/a, Aug. 2008. ISSN 15252027. doi: 10.1029/2008GC002009.

S. M. Carbotte, D. K. Smith, M. Cannat, and E. M. Klein. Tectonic and magmatic segmentation of the global ocean ridge system : a synthesis of observations. *Geological Society of London*, 2015.

Y. J. Chen and J. Lin. Mechanisms for the formation of ridge-axis topography at slow-spreading ridges: A lithospheric-plate flexural model. *Geophysical Journal International*, 136:8–18, 1999. ISSN 0956540X. doi: 10.1046/j.1365-246X.1999.00716.x.

E. Choi, L. Lavier, and M. Gurnis. Thermomechanics of mid-ocean ridge segmentation. *Physics of the Earth and Planetary Interiors*, 171(1-4):374–386, Dec. 2008. ISSN 00319201. doi: 10.1016/j.pepi.2008.08.010.

A. Dannowski, I. Grevemeyer, C. R. Ranero, G. Ceuleneer, M. Maia, J. P. Morgan, and P. Gente. Seismic structure of an oceanic core complex at the mid-atlantic ridge, 22 ° 19′n. *Journal of Geophysical Research*, 115(B7):B07106, July 2010. ISSN 0148-0227. doi: 10.1029/2009JB006943.

H. J. B. Dick, M. a. Tivey, and B. E. Tucholke. Plutonic foundation of a slow-spreading ridge segment: Oceanic core complex at kane megamullion, 23 °30′n, 45 °20′w. *Geochemistry, Geophysics, Geosystems*, 9(5):n/a–n/a, May 2008. ISSN 15252027. doi: 10.1029/2007GC001645.

J. Escartín, D. K. Smith, J. Cann, H. Schouten, C. H. Langmuir, and S. Escrig. Central role of detachment faults in accretion of slow-spreading oceanic lithosphere. *Nature*, 455(7214):790–794, 2008. ISSN 0028-0836. doi: 10.1038/nature07333.

D. A. Ferrill, J. A. Stamatakos, D. Sims, J. P. e. Evans, and S. H. e. Treagus. Normal fault corrugation; implications for growth and seismicity of active normal faults\rquestions in structural geology; 20th anniversary special issue. *Journal of Structural Geology*, 21 (8-9):1027–1038, 1999.

C. M. R. Fowler. *The solid earth: an introduction to global geophysics*. Cambridge University Press, 2004.

C. B. Grimes, B. E. John, M. J. Cheadle, and J. L. Wooden. Protracted construction of gabbroic crust at a slow spreading ridge: Constraints from 206pb/238u zircon ages from atlantis massif and iodp hole u1309d (30 °n, mar). *Geochemistry, Geophysics, Geosystems*, 9(8), 2008. ISSN 15252027. doi: 10.1029/2008GC002063.

G. Ito and M. D. Behn. Magmatic and tectonic extension at mid-ocean ridges: 2. origin of axial morphology. *Geochemistry, Geophysics, Geosystems*, 9(9):n/a–n/a, Sept. 2008. ISSN 15252027. doi: 10.1029/2008GC001970.

S. Kirby and A. K. Kronenberg. Rheology of the lithosphere: Selected topics. *Reviews of Geophysics*, 25(6):1219–1244, 1987.

L. L. Lavier, W. R. Buck, and A. N. B. Poliakov. Factors controlling normal fault offset in an ideal brittle layer. *Journal of Geophysical Research*, 105(B10):23431, 2000. doi: 10.1029/2000JB900108.

J. Lin, G. M. Purdy, H. Schouten, J.-C. Sempere, and C. Zervas. Evidence from gravity data for focused magmatic accretion along the Mid-Atlantic Ridge. *Nature*, 344:627–632, 1990. ISSN 0028-0836. doi: 10.1038/344627a0.

C. MacLeod, R. Searle, B. Murton, J. Casey, C. Mallows, S. Unsworth, K. Achenbach, and M. Harris. Life cycle of oceanic core complexes. *Earth and Planetary Science Letters*, 287(3-4):333–344, Oct. 2009. ISSN 0012821X. doi: 10.1016/j.epsl.2009.08.016.

J.-A. Olive, M. D. Behn, and B. E. Tucholke. The structure of oceanic core complexes controlled by the depth distribution of magma emplacement. *Nature Geoscience*, 3(7):491–495, June 2010. ISSN 1752-0894. doi: 10.1038/ngeo888.

J.-a. Olive, M. D. Behn, and L. C. Malatesta. Modes of extensional faulting controlled by surface processes. *Geochemistry Geophysics Geosystems*, pages 1–9, 2014. doi: 10.1002/2014GL061507.

T. J. Reston and K. G. McDermott. Successive detachment faults and mantle unroofing at magma-poor rifted margins. *Geology*, 39(11):1071–1074, Oct. 2011. ISSN 0091-7613. doi: 10.1130/G32428.1.

T. J. Reston and C. R. Ranero. The 3-d geometry of detachment faulting at mid-ocean ridges. *Geochemistry, Geophysics, Geosystems*, 12(7):n/a–n/a, July 2011. ISSN 15252027. doi: 10.1029/2011GC003666.

W. B. F. Ryan, S. M. Carbotte, J. O. Coplan, S. O'Hara, A. Melkonian, R. Arko, R. A. Weissel, V. Ferrini, A. Goodwillie, F. Nitsche, J. Bonczkowski, and R. Zemsky. Global multi-resolution topography synthesis. *Geochemistry, Geophysics, Geosystems*, 10, 2009. ISSN 15252027. doi: 10.1029/2008GC002332.

J.-C. Sempéré, J. Lin, H. S. Brown, H. Schouten, and G. M. Purdy. Segmentation and morphotectonic variations along a slow-spreading center : The mid-atlantic ridge (24 $^{\circ}00\,'$ n $\sim$ 30 $^{\circ}$ 40 $'$ n). *Marine Geophysical Researches*, pages 153–200, 1993.

D. K. Smith, J. R. Cann, and J. Escartín. Widespread active detachment faulting and core complex formation near 13 degrees n on the mid-atlantic ridge. *Nature*, 442(7101): 440–3, July 2006. ISSN 1476-4687. doi: 10.1038/nature04950.

D. K. Smith, J. Escartín, H. Schouten, and J. R. Cann. Fault rotation and core complex formation: Significant processes in seafloor formation at slow-spreading mid-ocean ridges (mid-atlantic ridge, 13 °-15 °n). *Geochemistry, Geophysics, Geosystems*, 9(3): n/a–n/a, Mar. 2008. ISSN 15252027. doi: 10.1029/2007GC001699.

D. K. Smith, H. Schouten, H. J. B. Dick, J. R. Cann, V. Salters, H. R. Marschall, F. Ji, D. Yoerger, A. Sanfilippo, R. Parnell-turner, C. Palmiotto, A. Zheleznov, H. Bai, W. Junkin, B. Urann, S. Dick, M. Sulanowska, P. Lemmond, and S. Curry. Development and evolution of detachment faulting along 50 km of the mid-atlantic ridge near 16.5°n. *Geochemistry Geophysics Geosystems*, pages 4692–4711, 2014. doi: 10.1002/2014GC005563.Received.

J. E. Spencer. Geologic continuous casting below continental and deep-sea detachment faults and at the striated extrusion of sacsayhuaman, peru. *Geology*, 27(4):327–330, 1999. ISSN 00917613. doi: 10.1130/0091-7613(1999)027⟨0327:GCCBCA⟩2.3.CO;2.

M. Tolstoy, A. J. Harding, and J. A. Orcutt. Crustal Thickness on the Mid-Atlantic Ridge: Bull's-Eye Gravity Anomalies and Focused Accretion. *Science*, 262(October):726–729, 1993. ISSN 0036-8075. doi: 10.1126/science.262.5134.726.

B. E. Tucholke and J. Lin. A geological model for the structure of ridge segments in slow spreading ocean crust. *Journal of Geophysical Research*, 99(B6):11937, 1994. ISSN 0148-0227. doi: 10.1029/94JB00338.

B. E. Tucholke, J. Lin, and M. C. Kleinrock. Megamullions and mullion structure defining oceanic metamorphic core complexes on the mid-atlantic ridge. *Journal of Geophysical Research*, 103(B5):9857, 1998. ISSN 0148-0227. doi: 10.1029/98JB00167.

B. E. Tucholke, M. D. Behn, W. R. Buck, and J. Lin. Role of melt supply in oceanic detachment faulting and formation of megamullions. *Geology*, 36(6):455, 2008. ISSN 0091-7613. doi: 10.1130/G24639A.1.

D. L. Turcotte and G. Schubert. *Geodynamics*. Cambridge, 2002.

D. L. Whitney, C. Teyssier, P. Rey, and W. R. Buck. Continental and oceanic core complexes. *Geological Society of America Bulletin*, 125(3-4):273–298, Dec. 2012. ISSN 0016-7606. doi: 10.1130/B30754.1.

M. S. Wong and P. B. Gans. Geologic, structural, and thermochronologic constraints on the tectonic evolution of the sierra mazatán core complex, sonora, mexico: New insights into metamorphic core complex formation. *Tectonics*, 27(4):1–31, 2008. ISSN 02787407. doi: 10.1029/2007TC002173.

M. Xu, J. P. Canales, B. E. Tucholke, and D. L. DuBois. Heterogeneous seismic velocity structure of the upper lithosphere at kane oceanic core complex, mid-atlantic ridge. *Geochemistry, Geophysics, Geosystems*, 10(10):n/a–n/a, Oct. 2009. ISSN 15252027. doi: 10.1029/2009GC002586.